# Small-scale dosimetry methods for normal tissues after radioembolization and peptide receptor radionuclide therapy

- a focus on the liver parenchyma and bone marrow

Jens Hemmingsson

Department of Medical Radiation Sciences
Institute of Clinical Sciences at Sahlgrenska Academy
University of Gothenburg

UNIVERSITY OF
GOTHENBURG

Gothenburg, Sweden, June 2023

Cover illustration by Jens Hemmingsson (Created with BioRender.com)

Small-scale dosimetry methods for normal tissues after radioembolization and peptide receptor radionuclide therapy- a focus on the liver parenchyma and bone marrow

© Jens Hemmingsson 2023
jens.hemmingsson@gu.se

ISBN: 978-91-8069-173-4 (Print)
ISBN: 978-91-8069-174-1 (PDF)

Printed by Stema Specialtryck AB, Borås, Sweden 2023

Till Henning, Nils och farmor

# ABSTRACT

Radionuclide therapies are increasingly used in cancer treatments as they have been proven to be both effective and safe. As biodistributions and uptake vary widely between patients, a standardized approach is bound to leave a fraction of patients overtreated or undertreated. Dosimetry-based evidence suggests treatment regimens could be improved on a patient-specific basis as the absorbed dose limits for critical organs are not always reached. This thesis has investigated two radionuclide therapies with distinctly different targeting mechanisms and has aimed at investigating the absorbed dose distributions in tumor tissue and the parenchyma of the liver after radioembolization and the radiosensitive red marrow after peptide receptor radionuclide therapy (PRRT).

In the first study, a patient with hepatocellular carcinoma underwent radioembolization prior to tumor resection with the aim of reducing the probability of tumor recurrence within the resection boundaries. Using SPECT images, autoradiography, and biopsies, the absorbed dose distribution was evaluated. The analysis revealed a low absorbed dose and a small coefficient of variation in the liver parenchyma. However, the distribution in the tumor showed high levels of heterogeneity, with the greatest accumulation of microspheres found in viable tumor tissue.

The three consecutive studies (II-IV) focused on the absorbed dose to the red marrow after PRRT. Since terbium-161, a radionuclide with a considerable emission of low-energy electrons, may be better suited to treat disseminated disease than lutetium-177 and yttrium-90, the second study focused on using an existing model of the bone marrow to investigate potential implications of bone marrow irradiation from terbium-161. The results demonstrated a strong dependence on the source distribution for terbium-161 due to the short range of the low-energy electrons while simultaneously indicating an increased absorbed dose to the red marrow compared to lutetium-177. The third study investigated the presence of somatostatin receptor subtype 2 (SSTR2) on $CD34^+$ stem and progenitor cells in the bone marrow. After the first treatment cycle with [$^{177}$Lu]Lu-DOTATATE, four SPECT/CT images were acquired for 17 patients with neuroendocrine neoplasms. The $T_9$-$L_5$ vertebrae, hip bones, thoracic aorta, and subcutaneous adipose tissue, along with a single tumor, were delineated in each patient. A compartment model was used to separate the contribution from blood-based activity and demonstrated prolonged retention in the bone marrow cavities for all patients and skeletal sites. These results inspired the development of a small-scale dosimetry model of the bone marrow in the fourth study to investigate how $CD34^+$ stem and progenitor cells are irradiated by uptake related to the expression of SSTR2. The model utilized previously described spatial distributions of $CD34^+$ stem and progenitor cells

to demonstrate an increased absorbed dose from terbium-161 compared to lutetium-177.

In conclusion, our results help to explain the observed hematological toxicities after [$^{177}$Lu]Lu-DOTATATE therapy by demonstrating a specific uptake in the radiosensitive bone marrow. As upcoming clinical trials with terbium-161 may result in a shift from lutetium-177 in somatostatin receptor-based radionuclide therapies, we used these findings to show that this can lead to increased irradiation of the red marrow.

# SAMMANFATTNING PÅ SVENSKA

Användningen av radionuklidterapier vid cancerbehandling har ökat stadigt under det senaste decenniet och framstår allt mer som en säker och effektiv behandlingsform. Trots att behandlingens effekt och dess biverkningar varierar mycket mellan patienter ges en del radionuklidterapier i på förhand fastställda doser. Detta innebär att en del patienter blir underbehandlade medan andra får allvarliga biverkningar. Studier har pekat på potentialen i dosimetri-baserad behandlingsoptimering där mängden radiofarmaka och antal behandlingscykler bestäms av den individuella patientens stråldos till riskorgan. Syftet med den här avhandlingen har varit att karakterisera stråldosfördelningen i tumör- och normalvävnad vid radioembolisering och i den strålkänsliga benmärgen efter peptidreceptor-radionuklidterapi (PRRT).

Det första arbetet analyserar dosfördelningen efter radioembolisering i en patient med hepatocellulärt carcinom. Radioembolisering är en leverspecifik behandling där mikrosfärer med radionukliden yttrium-90 injiceras i leverartären och färdas med blodet tills de ansamlas och fastnar djupt inne i artärträdet. Kirurgi användes för att ta bort tumören efter behandling och påföljande analys visade en mycket heterogen mikrosfärsfördelning sett till hela tumören med lokalt höga stråldoser till livskraftig tumör. Normalvävnaden som omgav tumören visade betydligt lägre stråldos och mindre spridning i mikrosfärsfördelningen.

Resterande arbeten fokuserade på metoder för att uppskatta stråldosen till den röda benmärgen vid PRRT. Detta är viktigt eftersom hematologisk toxicitet kan begränsa behandlingen och tidigare studier har korrelerat stråldosen till röd benmärg med hematologisk respons. Det andra arbetet jämförde stråldosen till röd benmärg med hjälp av en existerande benmärgsmodell. Ett potentiellt alternativ till lutetium-177 vid PRRT är terbium-161 som emitterar fler elektroner med kort räckvidd vid varje sönderfall och därför skulle kunna vara mer effektiv. Studien visade att stråldosen till den röda benmärgen från terbium-161 påverkas mer av dess fördelning i benmärgen än för lutetium-177, men att stråldosen från terbium-161 generellt är högre vid samma aktivitet.

Ett karakteristiskt drag hos neuroendokrina tumörer är ett överuttryck av somatostatinreceptor subtyp 2 (SSTR2) som är den molekylära måltavlan vid behandling med [$^{177}$Lu]Lu-DOTATATE. Studier har visat att även strålkänsliga stamceller i röd benmärg uttrycker dessa receptorer och med hjälp av SPECT/CT-bilder från 17 patienter kunde vi påvisa att upptag och utsöndring av radionukliden från benmärgen följde samma mönster som i tumörer där vi vet att densiteten av SSTR2 är hög. Studier har visat att fördelningen av stamceller i benmärgen är heterogen och i det sista

arbetet togs en småskalig modell av en benmärgskavitet fram för att på detaljnivå kunna studera stråldosfördelningen kring stamcellerna i röd benmärg. Återigen jämfördes lutetium-177 med terbium-161 och modellen visade en högre stråldos för terbium-161 till stamcellernas cellkärnor.

Sammanfattningsvis visade samtliga studier på dosfördelningens heterogenitet efter radionuklidterapi. Då retentionen av aktivitet i benmärgen är högre än tidigare trott efter behandling med [$^{177}$Lu]Lu-DOTATATE bör detta tas i beaktning vid stråldosberäkningar till röd benmärg och vid planering av kliniska studier med somatostatinanaloger kopplade till terbium-161.

# LIST OF STUDIES

I. Jens Hemmingsson, Jonas Högberg, Johan Mölne, Johanna Svensson, Peter Gjertsson, Magnus Rizell, Olof Henrikson, Peter Bernhardt
*Autoradiography and biopsy measurements of a resected hepatocellular carcinoma treated with 90 yttrium radioembolization demonstrate large absorbed dose heterogeneities.*

Advances in Radiation Oncology 2018 Vol.3 Issue 3 Pages: 439-446

II. Jens Hemmingsson, Johanna Svensson, Nicholas P van der Meulen, Cristina Müller, Peter Bernhardt
*Active bone marrow S-values for the low-energy electron emitter terbium-161 compared to S-values for lutetium-177 and yttrium-90.*

EJNMMI Physics 2022 Vol.9 Issue 1 No: 65

III. Jens Hemmingsson, Johanna Svensson, Andreas Hallqvist, Katja Smits, Viktor Johanson, Peter Bernhardt
*Specific uptake in the bone marrow causes high absorbed red marrow doses during [$^{177}$Lu]Lu-DOTATATE treatment.*

Accepted in the Journal of Nuclear Medicine, May 3, 2023

IV. Jens Hemmingsson, Johanna Svensson, Andreas Hallqvist, Viktor Johanson, Johan Mölne, Nicholas P van der Muelen, Cristina Müller, Peter Bernhardt
*Bone marrow dosimetry model for receptor-based radiotherapies; comparison between lutetium-177 and terbium-161.*

Manuscript

# RELATED PUBLICATIONS

Johanna Svensson, Tobias Rydén, Linn Hagmarker, Jens Hemmingsson, Bo Wängberg, Peter Bernhardt

*A novel planar image-based method for bone marrow dosimetry in (177)Lu-DOTATATE treatment correlates with haematological toxicity.*

EJNMMI Phys 2016 Vol. 3 Issue 1 No: 21

Tobias Rydén, Jakob Heydorn Lagerlöf, Jens Hemmingsson, Ida Marin, Johanna Svensson, Magnus Båth, P. Gjertsson, Peter Bernhardt

*Fast GPU-based Monte Carlo code for SPECT/CT reconstructions generates improved Lu-177 images.*

EJNMMI Physics 2018 Vol.5 Issue 1 No: 1

Peter Bernhardt, Johanna Svensson, Jens Hemmingsson, N. P. van der Meulen, J. R. Zeevaart, M. W. Konijnenberg, C. Müller, Jon Kindblom

*Dosimetric analysis of the short-ranged particle emitter 161-tb for radionuclide therapy of metastatic prostate cancer.*

Cancers 2021 Vol. 13 Issue 9 Pages 2011

# CONTENTS


**ABBREVIATIONS** 1

**INTRODUCTION** 3

Liver cancer ... 3
Neuroendocrine tumors ... 3
Radionuclides ... 4
Beta particles ... 4
Auger electrons ... 5
Internal conversion electrons ... 5
Bremsstrahlung photons ... 5
Linear energy transfer ... 5
Yttrium-90 ... 6
Lutetium-177 ... 6
Terbium-161 ... 7
The Monte Carlo method ... 9
Imaging ... 13
Reconstructions ... 14
Quantitative SPECT ... 15
Dosimetry in radionuclide therapy ... 15
Bone marrow ... 16
Hepatic radioembolization ... 17
Before therapy- Imaging ... 19
Before therapy- Dosimetry ... 20
After therapy- Imaging ... 20
After therapy- Dosimetry ... 21
Radiation-induced toxicity ... 21
Somatostatin receptor-based radionuclide therapy ... 22
Neuroendocrine tumors ... 22
Patient selection ... 23
Biodistributions ... 24
Bone marrow dosimetry ... 24
Skeletal dosimetry models ... 26
Dose-response relationship ... 27
Hematological toxicities ... 28
Small-scale dosimetry ... 29
Bone marrow quantification ... 30
Magnetic resonance ... 31
Computed tomography ... 32

**AIMS** 33

**PATIENTS AND METHODS** 35

Radioembolization 35

Dosimetry 36

Somatostatin receptor-based radionuclide therapy 36

Patients and imaging 36

Bone marrow dosimetry 37

Study II 37

Study III 39

Compartment model 39

Dosimetry 41

Study IV 42

**RESULTS AND DISCUSSION** 45

Study I 45

Study II 48

Study III 50

SSTR2 – Antagonists 55

Study IV 56

**CONCLUSIONS** 59

Study I – Radioembolization 59

Study II, III, IV – Bone marrow dosimetry 59

**FUTURE PERSPECTIVES** 61

**ACKNOWLEDGEMENTS** 63

**REFERENCES** 65

# ABBREVIATIONS

| | |
|---|---|
| $^{177}$Lu | Lutetium-177 |
| $^{90}$Y | Yttrium-90 |
| AF | Absorbed fraction |
| AM | Active (red) marrow |
| BMM | Bone marrow model |
| CCC | Cholangiocellular carcinoma |
| CDF | Cumulative distribution function |
| CT | Computer Tomography |
| CV | Coefficient of variation |
| GEP | Gastrointestinal tract and pancreas |
| HCC | Hepatocellular carcinoma |
| HCT | Hematocrit |
| IM | Inactive (yellow) marrow |
| MC | Monte Carlo |
| mCRC | Metastatic colorectal cancer |
| NEN | Neuroendocrine neoplasms |
| NET | Neuroendocrine tumors |
| OSEM | Ordered subset expectation maximization |
| PDF | Probability distribution function |
| PET | Positron emission tomography |
| RMBLR | Red marrow-to-blood ratio |
| RMECFF | Red marrow extracellular fluid fraction |
| SAF | Specific absorbed fraction ($g^{-1}$) |
| SCM | Single-cell model |
| SPECT | Single Photon Emission Computer Tomography |
| SSTR | Somatostatin receptors |
| TBS | Trabecular bone surface |
| TBV | Trabecular bone volume |
| TNC | Tumor-to-normal tissue concentration ratio |
| UFHADF | University of Florida Adult Female Phantom |
| UFHADM | University of Florida Adult Male Phantom |
| VOI | Volume of interest |

# INTRODUCTION

This thesis involves two radionuclide therapies utilized for treating liver tumors and neuroendocrine tumors. While providing an overview of the fundamental principles of these treatment modalities, this introduction primarily concentrates on discussing the normal tissue dosimetry involved in radioembolization and peptide receptor radionuclide therapy.

## Liver cancer

Primary liver cancer develop in the liver and is the third leading cause of cancer-related death and the sixth most common form of cancer globally (1). Three types of primary liver cancers exist; hepatocellular carcinoma (HCC), cholangiocarcinoma (CCC) in the bile ducts and angiosarcoma in the blood vessels. Originating in the hepatocytes, HCC is the most prevalent primary liver cancer accounting for approximately 90% of cases (2). Along with excessive alcohol use, Hepatitis B or C viral infections are major risk factors for developing HCC (3). A cirrhotic liver, which is a consequence of the mentioned risk factors, is particularly vulnerable as the cellular response to chronic damage distorts the hepatic structure and impairs tumor-suppressing efforts (2). For patients diagnosed with HCC in the US, the five-year survival rate was less than 20% during the years 2010-2014 (4). However, the main part of all hepatic tumors are metastases from other origins and it is expected that up to 25% of all cancer patients will develop these (5). Treatment options vary depending on the type, stage and grade of the cancer but liver transplantation, resection or radiofrequency ablation are potentially curative treatments. Other treatment options are palliative or symptomatic but can also aim at restaging the disease to enable curative treatments (6).

## Neuroendocrine tumors

Neuroendocrine neoplasms (NENs) are a diverse group of tumors that originate from the diffuse neuroendocrine cell system. While these tumors can develop in various parts of the body, they most commonly occur in either the lungs (22-27%) or the gastrointestinal tract and pancreas (62-67%) (GEP) (7). Besides inheritance, high body mass index, diabetes, smoking and alcohol are identified as risk factors for developing NENs (8). NENs are typically classified as slow-growing low-grade malignancies (Grade 1), leading to a relatively high prevalence, but also comprise aggressive high-grade tumors (Grade 3). Accurate classification is important as the expected overall survival time varies greatly depending on the grade, stage and origin from over 20 years (median) for G1 to less than a year (median) for rapidly proliferating G3/G4 grade tumors in the lung (9). Although NENs are rare relative to other forms of cancers accounting for less than 2% of all malignant tumors, the incidence has been increasing to 6.4 and 8.6 per 100 000 for the US and UK, respectively (9, 10). The increase in incidence is

mainly attributed to heightened diagnostic awareness but could also involve an actual increase (11). At the time of diagnosis, approximately 20% of patients have metatases with a clear preference to metastasize in the liver which is also associated with a poor prognosis (12). For patients with unresectable NENs in particular, systemic treatments can offer increased survival and ameliorate symptoms.

## Radionuclides

Depending on the targeting mechanism, radionuclide therapies can be delivered either loco-regionally or systemically, with the aim of delivering cytotoxic radiation to cancer cells. An additional feature of many of the radionuclides most frequently used is imaging of the pharmaceutical distribution within the patient, which has become an important tool to evaluate and improve treatments.

### Beta particles

A surplus of neutrons or protons in an atomic nucleus can be transformed through beta decay or electron capture by converting a proton into a neutron or vice versa. In beta decay, either an electron ($\beta^-$) or a positron ($\beta^+$) is generated and emitted, depending on the direction of the conversion. In the case of electron capture, an orbital electron is absorbed. Beta particles are emitted with energies from a continuous distribution (Fig. 1) a result of the co-emission of a neutrino, where the beta spectrum energies depend on the mass differences between initial and final states (Q value). Generally, beta decay is accompanied by the emission of gamma-ray photons.

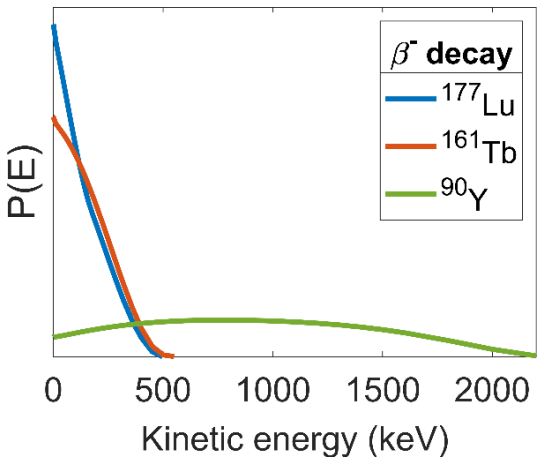


***FIGURE 1**. Beta particle spectra for lutetium-177, terbium-161, and yttrium-90, where the y-axis represents the energy dependent emission probability.*

### Auger electrons

X-ray photons are emitted when orbital electrons from higher energy levels fill inner vacancies. Instead of x-ray emission, the excess energy can be transferred to an orbital electron which is emitted with the characteristic energy of the electron transition minus the binding energy of the emitted orbital electron (Fig. 4). These low-energy electrons are referred to as Auger (or Auger/Meitner) electrons or Coster-Kronig/super Coster-Kronig electrons depending on the relation between vacancy shell and emission shell. In this thesis, all electron emissions arising from this process are referred to as Auger electrons.

### Internal conversion electrons

An excited atomic nucleus may transfer its excess energy to an orbital electron which is then ejected from the atom. Internal conversion occurs in competition with gamma emission and results in characteristic electron energies that depend on the binding energy of the emitted orbital electron (Fig. 4). The vacancy in the electron shell is filled causing subsequent emissions of x-rays or Auger electrons.

### Bremsstrahlung photons

Electrons lose energy either through inelastic collisions or bremsstrahlung emissions. The probability of bremsstrahlung emission is approximately proportional to the square of the charge of the absorber nucleus, leading to relatively few bremsstrahlung emissions in soft tissue. The electron can potentially lose all kinetic energy to a single bremsstrahlung photon although the majority of emissions will have lower energies (Fig. 3C). The bremsstrahlung yield, i.e. the number of photons emitted per beta decay, is the average fraction of the initial kinetic energy that is released as bremsstrahlung photons during the deceleration.

### Linear energy transfer

The average energy that an electron deposits per distance travelled, the linear energy transfer (LET) is dependent on the kinetic energy of the electron and the material traversed. This is a quantity of particular interest in radionuclide therapies as high LET is correlated to an increased probability of inducing multiple double-strand breaks and consequently an increased probability of cell death (13). Low-energy electrons, for which energy there is no well-defined threshold, have an increased LET compared to the average emitted $\beta^-$ particle which means they deposit more energy per travelled distance, a potentially attractive feature for therapeutic purposes. By determining an energy threshold for secondary electrons a constraint can be set for what is to be considered “locally absorbed energy”. Secondary electrons with kinetic energies above the threshold are likely to deposit energy outside a pre-determined region of interest and will therefore be excluded from the energy deposition tally (Fig. 2).

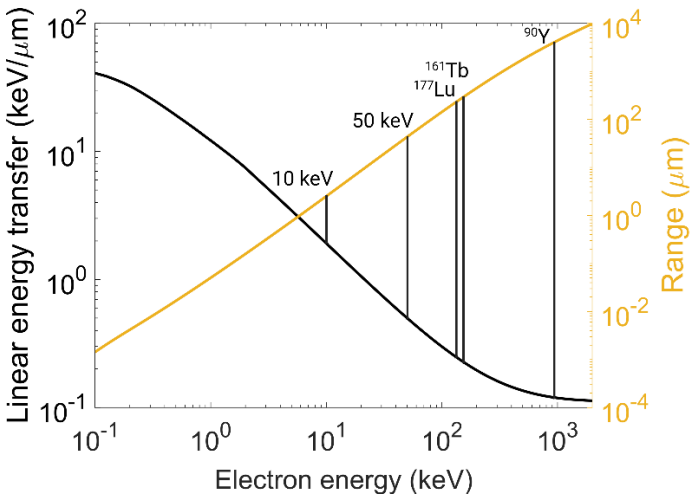


***FIGURE 2**. The linear energy transfers and corresponding average range for electrons in soft tissue. The bars indicate energies for electrons with kinetic energies of 10 keV, 50 keV and average beta-particle energies for lutetium-177, terbium-161 and yttrium-90.*

## Yttrium-90

Yttrium-90 can be considered a pure high-energy beta-emitter as the branching ratios for additional charged particle emissions are negligible in terms of dosimetry (Table 1). The $\beta^-$ decay to excited states of zirconium-90 occur with total branching fractions of 0.017, mainly resulting in emission of gamma photons with energies 1760.7 keV. However, the resulting emission of bremsstrahlung photons is considerable and can be utilized for single-photon emission computed tomography (SPECT) imaging. From the $0^+$ excited state of zirconium-90, with a branching fraction of $31.86 \cdot 10^{-6}$, internal pair-production occurs resulting in positron emission and consequently 511 keV photons that enable positron emission tomography (PET) imaging (14).

## Lutetium-177

Lutetium-177 has several useful characteristics of a theranostic radionuclide. Approximately 21% of decays go to excited states of 177-hafnium where multiple photons with energies suitable for imaging are emitted, enabling diagnostics and simplifying dosimetry (Table 1). The photon primarily used in SPECT imaging has an energy of 208.4 keV resulting in a mean free path of approximately 7.45 cm in soft tissue. Compared to yttrium-90, the beta particles and additional 1.17 low-energy electrons (< 50 keV) emitted per decay contribute to a highly localized energy deposition.

## Terbium-161

In relation to lutetium-177, the interest in terbium-161 is essentially due to two desirable properties (Table 1). Firstly, as a member of the same group in the periodic table of elements as lutetium, the lanthanides, the chemical properties of terbium-161 translate to enable the use of procedures developed for lutetium-177. This has been shown in a 2020 preclinical study and is highly attractive as the step into clinical trials is somewhat shortened (15). Secondly, although the $\beta^-$ spectra are similar (Fig. 1), terbium-161 emits an additional 12.38 Auger and conversion electrons (Table 1) below 50 keV per decay (16).

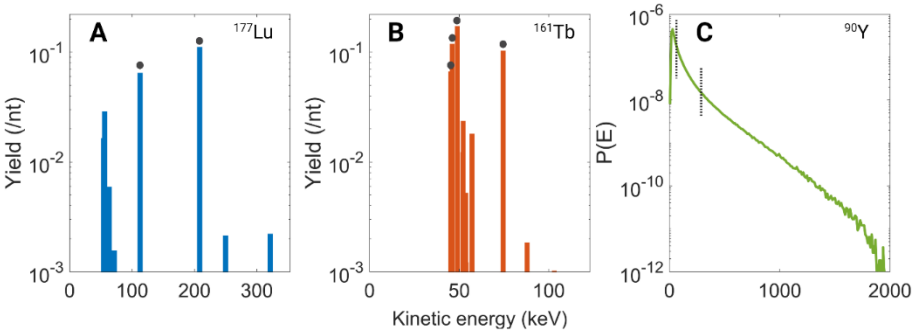


***FIGURE 3**. Photon emissions from lutetium-177 (A) and terbium-161 (B) with yields above $10^{-3}$ (photons emitted per decay). Photons most suitable for SPECT imaging are highlighted with a black dot. Shown in panel C is the continuous bremsstrahlung emission spectrum from yttrium-90 in soft tissue that enables SPECT imaging with the corresponding probability on the y-axis. The dashed lines in panel C show the energy window used for SPECT imaging in study I (16).*

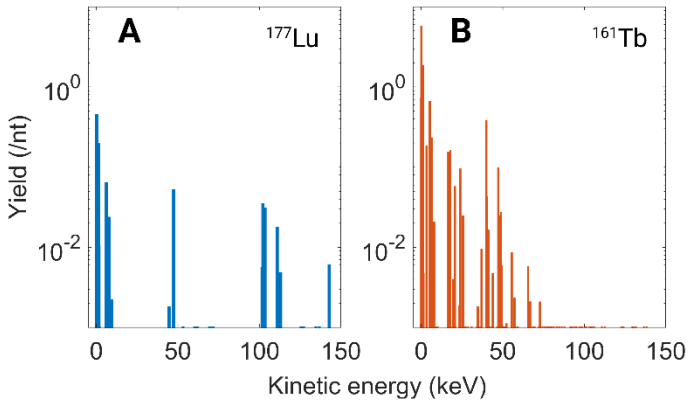


***FIGURE 4**. Auger and internal conversion electrons with yields over $10^{-3}$ emitted by lutetium-177 (A) and terbium-161 (B). Yttrium-90 does not emit additional electrons with sufficiently high yields and is not presented (16).*

***TABLE 1***

*Characteristics of the radionuclides used in this thesis*

| | **Yttrium-90** | **Lutetium-177** | **Terbium-161** |
|---|---|---|---|
| Half-life (d) | 2.668 | 6.647 | 6.892 |
| **Beta particle energy (keV)** | | | |
| Max | 2278.7 | 498.3 | 592.9 |
| Mean | 933 | 133 | 154 |
| **Beta particle range (cm)** | | | |
| Max | 1.135 | 0.176 | 0.223 |
| Mean | 0.402 | 0.023 | 0.029 |
| **Yield of Auger and Internal conversion electrons per decay (keV/decay)** | | | |
| < 50 keV | 0.0013 | 1.17 | 12.4 |
| < 10 keV | 0.0012 | 1.12 | 11.1 |
| < 1 keV | 0.0011 | 0.82 | 8.10 |

## The Monte Carlo method

There are a number of Monte Carlo (MC) programs freely available and currently used in the field of medical physics of which several are open source. Photon and electron transport is most commonly supported; what particles can be simulated besides these vary between codes. Although new programs crop up continuously, some of the most frequently used in medical physics are the CERN-developed GEANT4 with the sister program GATE, developed specifically for medical applications, PENELOPE, EGSnrc, the MCNP6 and Fluka.

PENELOPE supports photon, electron and positron transport through arbitrary materials and geometries for energies ranging between 50 eV and 1 GeV (17). By adjusting the variables in Table 2, users can easily customize PENELOPE to enable event-by-event simulation, condensed histories, or a combination of both. Radionuclide sources can be included in the simulation through the PENNUC extension and many radionuclides are available for download from Laboratoire National Henri Becquerel (18). Furthermore, the recently developed PENH and PenRed extensions have enabled proton transport simulations and parallelization of the PENELOPE code (19, 20). Extensive simulations times are often necessary to decrease the variance in complex MC calculations, which can be problematic in frequently used clinical applications. However, parallel computing can substantially reduce these times. PENELOPE is the MC engine mainly used for simulations in this thesis.

***TABLE 2***

*User-defined values to determine simulation speed and accuracy in PENELOPE*

| Variable | Description | Parameter settings in Fig.5 |
|---|---|---|
| $E_{Abs}$ | Absorption energies (> 50 eV) for photons, electrons and positrons, set separately for each particle type (eV) | 200 eV |
| $C_1$, $C_2$ | Elastic scattering parameters for the first transport mean free path that defines a critical angle ($C_1$) and energy loss ($C_2$) during a step at which the interaction is defined as hard (0-0.2) | 0.01,0.01 |
| $W_{CC}$ | Cutoff energy for inelastic collisions of electrons and positrons | 200 eV |
| $W_{CR}$ | Cutoff energy for bremsstrahlung emission of electrons and positrons | 200 eV |

The MC method has proven incredibly useful in the field of radiation transport as many of the processes involved are well described by physics. Photons are effectively transported since few interactions (≤ 20) take place from emission to absorption via Compton and Rayleigh interactions to photoabsorption. Although an electron can lose half of its kinetic energy to orbital electrons or all kinetic energy through bremsstrahlung emission the overwhelmingly dominant interaction is elastic with small energy losses and scattering angles. This leads to a very large number of interactions for single electrons and consequently long computation times (Fig. 5) (21). In PENELOPE, this is handled through mixed simulations, offering detailed simulations for particles below predefined thresholds that are determined for each simulation by setting appropriate values to the variables in Table 2.

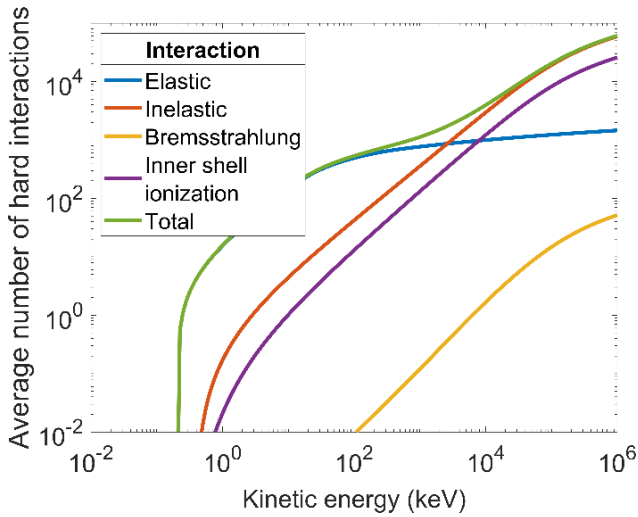


***FIGURE 5***. *The average number of hard interactions for electrons of a specific energy traversing soft tissue. The figure is calculated using the parameters of Table 2.*

The principle behind the MC method is to generate stochastic values attributed to a probability distribution. Because the input is a random number, the output will accurately represent the process described by the probability distribution function (PDF) for a sufficiently large sample size. The random number generator is the engine of the MC method, responsible for producing uniform uncorrelated random numbers between 0-1. Random number generators of sufficient quality are available for all programming languages.

The performance of an MC engine is partly defined by the sampling efficiency as the path of a single particle can involve multiple samplings from energy-dependent distributions. Several approaches of varying complexity have been developed for efficient sampling. The rejection method and importance method both utilizes the PDF for sampling (Fig. 6). The rejection method basically functions by throwing a digital dart at the PDF, accepting the sample every time the PDF is hit. This can become highly inefficient for narrow distributions in which case importance sampling can be applied. The methodology is similar but darts are only thrown on regions contributing significantly to the area of the PDF thereby increasing the hit rate. Of course, the important region has to be predefined and representative of the whole distribution if the method is to generate realistic results.

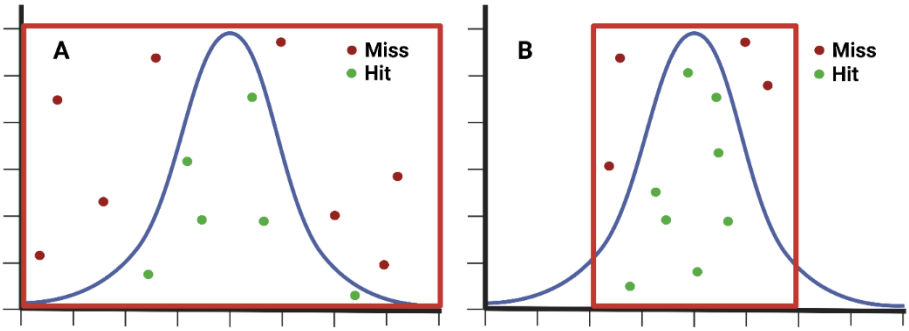


***FIGURE 6**. The rejection method (A) and the importance method (B) both utilize two random numbers to represent a coordinate within the red box. A green dot inside the blue function is a hit representing a sampled value and a red dot corresponds to a miss and the sampling process is repeated. Created with BioRender.com.*

However, sampling a value directly from the PDF is often inefficient. This can be managed by first calculating the cumulative distribution function (CDF) i.e. a non-decreasing function between 0-1, and then proceeding to calculate the inverse of the CDF. This method, called an inverse transformation, works best in cases where the PDF has a simple analytical expression (Eq. 1).

$$f(x) = e^{-\mu_{Tot}x}\mu_{Tot}dx \qquad \text{Eq. 1}$$

The sampling of a discrete step-length (s) for a photon traversing a material can be used to exemplify the inverse transformation method since the interaction probability of a photon is described by an exponential function and the total attenuation coef-

cient $\mu_{Tot}$. To be considered a PDF, a function f(x) typically has to be normalized as the interaction probability should integrate to 1 (Eq. 1).

The CDF is calculated by integrating the PDF between 0 and the step length, s, to be sampled (Eq. 2).

$$F(s) = \int_0^s e^{-\mu_{Tot}x}\mu_{Tot}dx = \mu_{Tot}\left[\frac{e^{-\mu_{Tot}x}}{-\mu_{Tot}}\right]_0^s = 1 - e^{-\mu_{Tot}s} \qquad \text{Eq. 2}$$

As can be seen in Eq. 2, F(s), is close to 0 for very small step lengths, s, and reaches 1 for long step lengths. The inverse CDF can be calculated by substituting F(s) with a uniform random variable ξ between 0-1, and solving for s (Eq. 3).

$$\xi = 1 - e^{-\mu_{Tot}s} \rightarrow s = \frac{\ln(\xi)}{\mu_{Tot}} \qquad \text{Eq. 3}$$

The sampling efficiency for the inverse transformation in Eq. 3 is 100% as each step is sampled directly from the PDF (Fig. 7). Using pure rejection sampling the corresponding sampling efficiency would have been approximately 20%.

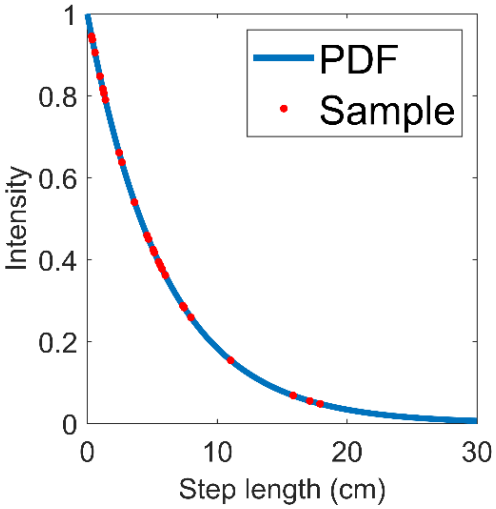


***FIGURE 7**. Visualization of the inverse transformation method for sampling of 25 photon path lengths randomly. Shown here for 100 keV photons in soft tissue.*

At each interaction point the type of interaction has to be determined by comparing a random number to the different fractions of interaction cross sections (Eq. 4).

$$\xi < \frac{\sigma_A}{\sigma_{A+B}} \qquad \text{Eq. 4}$$

If a particle deposits all energy at an interaction point it is discontinued and new particles emerging from the interaction can be followed analogously. For non-catastrophic interactions, a scattering angle and subsequent energy loss is sampled and the particle is transported to the next interaction site.

## Imaging

The potential for imaging associated with some of the radionuclides used for therapy is a clear advantage over other pharmaceuticals. Although perhaps mainly associated with cancer, radionuclide imaging is also used to assess myocardial perfusion, inflammation, lung ventilation, neuronal function in the brain and more. SPECT cameras operate at lower costs compared to PET, partially due to the short half-lives involved with PET tracers that require infrastructure for radionuclide production. Also, the longer physical half-life of SPECT radionuclides, which can be useful for individualizing treatments over multiple cycles, are better suited to study biological processes than their PET counterparts (22).

Ideally, an imaging radionuclide emits photons with high yields at single, high enough energies to minimize the attenuation in the patient yet low enough to limit the probability of septal penetration in the collimator. The purpose of the collimator is to discretize the underlying distribution of activity so that the origin of the photon can be discerned and the scintillation crystal is not overwhelmed with photons. The choice of collimator greatly affects the spatial resolution of reconstructed images through varying thicknesses as well as the size and shape of the parallel holes.

The basic principle of photon collection for scintillator detectors is to efficiently convert incoming gamma photons into visible light. This requires a material with a high linear attenuation coefficient for higher energies that is simultaneously translucent to visible light, classically thallium-activated sodium iodide NaI(Tl). The small initial electrical pulse from the photocathode, which is proportional to the incoming photon energy, is enhanced by a photomultiplier to create an electrical pulse that can be counted. More recently, cameras with solid-state semiconductor detectors have entered the clinic (23). These create electronic signals directly by applying a high voltage across a cadmium-zinc-telluride (CZT) material to collect electrons from ionizations.

While the spatial resolution demonstrates a system's ability to separate two sources, the energy resolution can be determined by fitting a Gaussian function to a peak in the collected energy spectrum and determining the full width at half maximum. These can vary substantially depending on the measurement settings and reconstruction parameters and a comparison between imaging systems is therefore not always straightforward. However, increased sensitivity and energy resolution has been reported for CZT systems compared to SPECT (24, 25).

## Reconstructions

The choice of reconstruction algorithm will impact the quality of the final image through the handling of attenuation correction and scattering and by affecting the noise levels and spatial resolution. The projections acquired for each set of camera angles around the patient are stacked as slices in a sinogram. In iterative reconstructions, which is the most frequently used SPECT reconstruction method, the principle is to create an estimate of each projection by modeling attenuation, scatter and collimator parameters. The ratio between the measurement and estimate is used to update the estimate in the next iteration. These steps are repeated until a predefined level of agreement is made between the estimate and measurement (26). Maximum likelihood expectation maximization (MLEM) is a statistical iterative algorithm that suppresses image noise by approximating the source distribution with a Poisson distribution in the estimate (27). To speed up the convergence of the estimate produced by the MLEM method, projections can be divided into subsets in a method called ordered subset expectation maximization (OSEM).

The inclusion of scattered photons in a measurement is a source of uncertainty as it degrades the quantitative accuracy and image contrast (28). For example, due to attenuation, some emitted photons of interest may fail to reach the detector. Additionally, those that do pass through the collimator aperture may have been scattered through the Compton or Rayleigh interaction, or they may have originated from different regions yet still managed to pass through the same hole of the collimator. Instead of using a window-based scatter correction to estimate and subtract the contribution of scattered photons in the emission window, a Monte Carlo-based approach can be applied by using the voxels in the co-registered CT to transport photons from the source voxel, through the collimator to the NaI(Tl) crystal. This computationally expensive procedure is possible due to improvements in computer hardware as well as variance reduction techniques (29). Commonly, and in the Sahlgrenska Academy reconstruction code (SARec), the photon transport is applied when the estimate is projected onto the detector plane (30). During this step further corrections based on line-source measurements are also applied; a Gaussian scattering kernel that details the

camera-specific scattering in the collimator, NaI(Tl) crystal and camera housing. The result is a reconstructed SPECT image with improved contrast and resolution (30).

### Quantitative SPECT

Besides the degrading factors involved in SPECT image collection and reconstruction, accurate quantification is also dependent on correct delineation of the volume of interest (VOI). This is considerably simplified by the co-registration of a CT at the time of the SPECT acquisition, as it enables precise delineation in regions of low uptake that would otherwise be impossible to accurately identify. However, the limited spatial resolution in SPECT images will influence what counts are attributed to the VOI as the activity in small structures or edge voxels is under- or overestimated to a varying extent (the partial volume effect) (31). This effect is typically addressed by a post-reconstruction correction derived through phantom measurements where known activity concentrations in spherical inserts are used to quantify the overlap between sphere and surroundings. In the dosimetry procedure, the partial volume effect is the main source of uncertainty along with the phantom-derived calibration factor that is used to convert the count rate in each voxel to activity (32).

## Dosimetry in radionuclide therapy

In general, dosimetry refers to the quantification or estimation of energy absorbed in a body after radiation exposure. For radionuclide therapies, the body of interest can vary from the whole body to targeted malignancies, organs or sub-regions of organs (33). To estimate the mean absorbed dose it is necessary to establish a source and target region as well as determine the deposited energy per decay, activity concentration, and biodistribution and target region mass. The formalism developed by the medical internal radiation dose (MIRD) committee has attempted to standardize dosimetry calculations (Eq. 5) (34, 35).

$$D(r_T, \tau) = \sum_{r_S} \tilde{A}(r_S, \tau)\, S(r_T \leftarrow r_S) \qquad \text{Eq. 5}$$

The time-independent mean absorbed dose to a target region ($r_T$) and integration time ($\tau$) is denoted by $D(r_T,\tau)$. The number of decays in the source region ($r_s$) during time $\tau$ is expressed by the time-integrated activity $\tilde{A}(r_S,\tau)$. The S-value, $S(r_T \leftarrow r_S)$, represents the mean absorbed dose to $r_T$ for a given unit of activity in the source region ($r_s$) (Eq. 6).

$$S(r_T \leftarrow r_S) = \frac{\sum_i E_i Y_i \, \varphi(r_T \leftarrow r_S, E_i)}{m(r_T)} \qquad \text{Eq. 6}$$

Where i represents a particular nuclear transition and its respective energy ($E_i$) and yield ($Y_i$). The deposited energy in $r_T$ with mass $m(r_T)$ from the i:th nuclear transition in $r_s$ is determined by the absorbed fraction ϕ. While the method can simplify comparisons between studies and datasets, it is necessary to acknowledge differences in published S-values, depending on the radionuclide data and phantoms used. This was demonstrated in the latest EANM dosimetry guidelines for lutetium-177 showing differences of 0.5% to 5% for electron and photon emissions, respectively (36).

Although not a prerequisite for treatments with [$^{177}$Lu]Lu-DOTATATE, the current standard practices for dosimetry at Sahlgrenska university hospital after treatment with [$^{177}$Lu]Lu-DOTATATE involves monitoring the total absorbed dose to the kidneys. The requirements from the European Medicines Agency state that the kidney function and status should be monitored through creatinine clearance and serum creatinine. This contrasts the recommendations of EURATOM stating that radiopharmaceutical treatments should be individually planned and verified (37). Tumor and bone marrow dosimetry are performed for research purposes only.

## Bone marrow

The bone marrow is located in the cavities of trabecular bone inside the cortical bone of the axial skeleton (Fig. 8). The central functions of the bone marrow are to produce blood cells and store fat. Blood cell production, the hematopoiesis, is hierarchical with hematopoietic stem cells at the top. Although very rare, roughly 70 cells in every million bone marrow cells, the stem cells have a unique ability for differentiation and self-renewal that sustains the hematopoietic system (38). The subsequent progenitor cells cannot self-renew to the same extent as the stem cells but are also multipotent after lineage commitment. The production of blood cells, i.e. erythrocytes, leukocytes and thrombocytes, is efficient and highly adaptable. Every second, about two million erythrocytes are generated, and the hematopoietically active (red) marrow obtains its characteristic red color from the presence of hemoglobin (39). As an individual age, the bone marrow undergoes changes in both composition and location. While infants have predominantly hematopoietically active bone marrow, adults typically have a higher proportion of adipose (yellow) marrow, with most of the red marrow concentrated in the hip bones, thoracic and lumbar vertebrae, ribs, scapulae, and sacrum. (40). However, this distribution can be altered by factors such as bone metastases or after chemotherapy or radiation therapy (41).

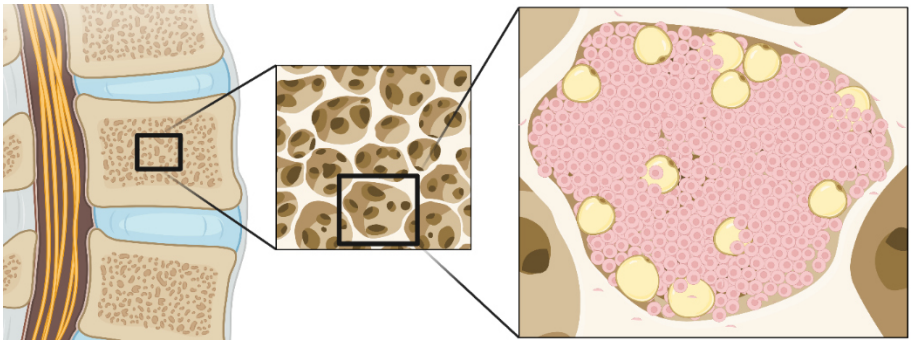

***FIGURE 8**. A simplified visualization of red and yellow bone marrow in a trabecular bone cavity in the lumbar vertebrae. Created with BioRender.com.*

One consequence of the bone marrow's proliferative capabilities is its sensitivity to stress (42). This is not only manifested by failure to repair DNA damage but also through a variety of cellular responses that potentially trigger apoptosis and deplete stem cell reserves (43). The radiosensitivity has been shown to vary greatly between individuals which adds to the difficulties in predicting the bone marrow response after radionuclide therapy (44).

## Hepatic radioembolization

The targeting principle in radioembolization is loco-regional and utilizes the dual blood supply of the liver to distribute microspheres to malignant cells within the liver. The hepatic artery supplies the liver with oxygenated arterial blood. Almost the whole gastrointestinal tract drains its venous blood, with all the absorbed products of digestion, into the liver via the portal vein (Fig. 9) (45). About 70–80% of the total blood flow through the normal liver parenchyma is supplied via the portal vein, while the remaining part comes from the hepatic artery. In contrast, the blood supply for hepatic tumors stems mainly from the arterial blood flow (46, 47). Angiography is a medical procedure in which a catheter is placed into an artery, (the hepatic artery in the case of hepatic angiography) or one of its branches under x-ray guidance. Through this catheter, microspheres can be distributed to the entire liver or selectively to a specific lobe or segment (Fig. 10). The microspheres then lodge mainly in the metastatic tissue as this is perfused almost entirely by arterial blood while the normal liver parenchyma is perfused only to a small degree by arterial blood. The microspheres have a diameter a few times larger than the diameter of the hepatic sinusoids and follow the arterial vessels until they become lodged. Slow injection prevents clustering and backflow into other parts of the liver or the duodenum and stomach.

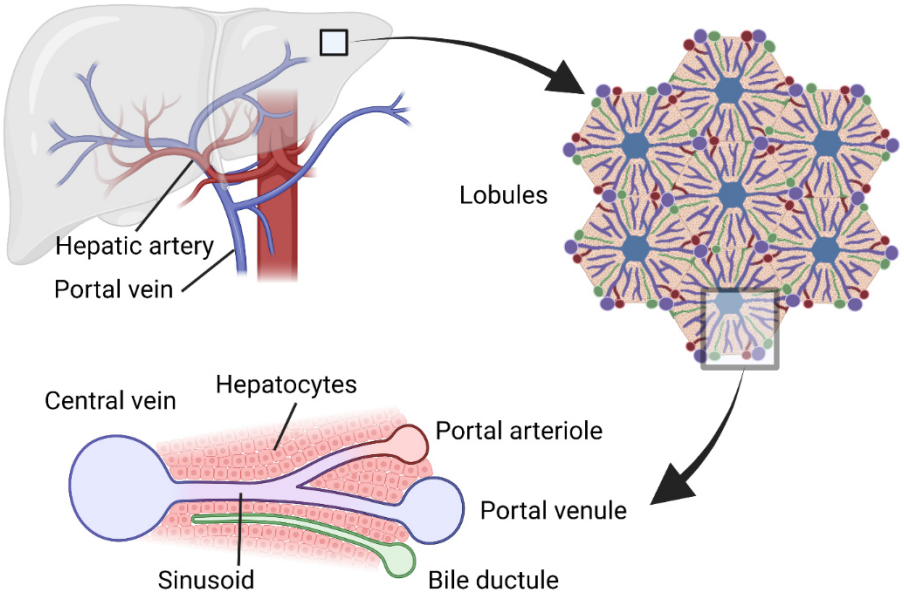


***FIGURE 9**. The hepatic parenchyma is organized in lobules that are supplied with blood from the both hepatic artery and portal vein. Sinusoids, a form of fenestrated capillaries, receive blood from arterioles and portal venules and drain into the central vein. Created with BioRender.com.*

To study the radiation exposure to the tumor and liver cells, the hepatic arterial structure has been modeled as a bifurcating tree with up to 20 generations of vessels with successively decreasing arterial diameters (48). A biopsy study of normal liver tissue after RE with resin microspheres demonstrated microsphere clustering in strings in the terminal arterioles and larger groups in small arteries, finding single microspheres as well as clusters of up to 450 spheres (49).

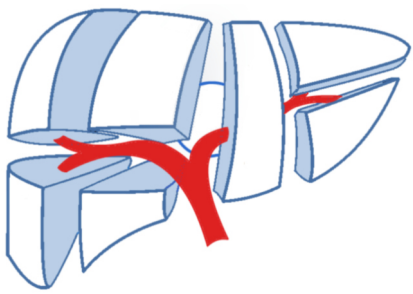

***FIGURE 10**. Liver anatomy can be classified into eight functionally independent segments using the Couinaud classification. Each segment has its unique vascular inflow, outflow, and biliary drainage, with a branch of the portal vein, hepatic artery, and bile duct located at the center.*

Currently, three different types of microspheres are available for radioembolization (Table 3); glass or resin microspheres with yttrium-90 or poly-L-lactic acid microspheres containing holmium-166 (TheraSphere®, SIR-Sphere® and QuiremSpheres®, respectively). Glass and holmium-166 microspheres are not further discussed in this thesis.

***TABLE 3***

*Microsphere characteristics for the three types commercially available (50)*

| Material | Activity per sphere (Bq) | Density ($g/cm^3$) | Diameter (µm) | | Spheres per GBq (million) |
|---|---|---|---|---|---|
| | | | Mean | Range | |
| Glass | 1250-2500 | 3.3 | 25 | 20-30 | 1.3 |
| Resin | 50 | 1.6 | 32.5 | 20-60 | 16 |
| Poly-L-lactic acid | 67-400 | 1.4 | 30 | 15-60 | 10 |

Radioembolization is primarily used for HCC, CCC and metastatic colorectal cancer (mCRC) but have been applied to other forms of cancer as well. Currently, there appears to be no across-the-board consensus on the efficacy of RE compared to other loco-regional or systemic treatments (51, 52). At the same time, several randomized trials have demonstrated favorable results for RE compared to chemotherapy for mCRC, HCC, and metastases of primary large bowel cancer either by including RE in the treatment protocol with chemotherapy or as a stand-alone treatment, showing increased progression-free survival and time to progression as well as less toxicity and a favorable tolerance (53, 54, 55, 56). Studies have also reported on the successful use of RE in downstaging patients for transplants or surgery (57, 58). While RE is considered a palliative treatment, these results are encouraging as surgery along with liver transplantation and radiofrequency ablation are the only curative options for primary liver cancers. The curative rates for these treatment options was described for HCC in a study recently, with 20-30% for ablation and liver resection and over 70% for liver transplantation (59).

## Before therapy - Imaging

Prior to the injection of microspheres, an angiography and a pre-therapeutic treatment simulation are performed using technetium-99m macroaggregated albumin ($^{99m}$Tc-MAA). The purpose of the angiography is to find and coil any vessels branching from the hepatic artery into the digestive system and to identify optimal catheter positions from where the microspheres can be injected safely (60). SPECT image acquisition is performed after administration of 75-150 MBq of $^{99m}$Tc-MAA and is preferable to planar images due to reported overestimations of the lung shunt fraction (61). The $^{99m}$Tc-MAA SPECT images can detect and quantify extrahepatic shunting of micro-

spheres, which often persists even after coiling extrahepatic vessels during the angiography procedure, into the lungs and gastrointestinal tract. The amount of activity can then be adjusted accordingly, to minimize the risk of radiation pneumonitis.

### Before therapy - Dosimetry

Dosimetry for radioembolization with yttrium-90 is image-based, either using a pre-therapeutic injection of technetium-99m albumin aggregated ($^{99m}$Tc-MAA) or on post-treatment SPECT or PET imaging. The recommendation in the latest EANM guidelines on RE is to perform both due to potential discrepancies between the distribution of MAA particles and microspheres (62). However, by assuming similarities in the distribution, $^{99m}$Tc-MAA SPECT images can be used in individual treatment planning by quantifying the uptake ratio between tumors and normal liver tissue to determine the prescribed activity in the multi-compartment method for resin microspheres (Eq. 7) (63). Although this approach is more laborious, the rationale has been deemed sensible compared to the other more rudimentary methods to determine the prescribed activity (64). Both the body surface area method for resin microspheres and mono-compartment (target) model from MIRD neglects any information on the activity distribution.

$$A[GBq] = D_{NL}\frac{TN_{ratio}m_T + m_{NL}}{50(1 - LSF)} \qquad \text{Eq. 7}$$

Where $D_{NL}$ is the specified absorbed dose to normal liver tissue, m is the tumor ($m_T$) and normal liver mass ($m_{NL}$) and 50 represents the deposited energy per GBq (J/GBq) assuming a uniform distribution of yttrium-90. Based on information from the $^{99m}$Tc-MAA SPECT, $TN_{ratio}$ is the uptake ratio between tumor and normal liver tissue and LSF is the fraction of counts in the lungs compared to the total number of collected counts in the liver and lungs.

### After therapy - Imaging

Several challenges are involved in SPECT imaging of yttrium-90. The continuous bremsstrahlung spectrum makes energy window setting difficult as no photopeak exists (Fig. 3C). Furthermore, the desirable photon energies have low probabilities while photon energies of up to 2270 keV can penetrate and scatter through the collimator to reduce image quality. However, CT-based scatter and attenuation correction can be applied and phantom studies have determined the most appropriate energy-window setting for quantification to be 90-120 keV with a high energy collimator (65, 66). Furthermore, MC-based SPECT reconstructions have proven effective for yttrium-90 by further controlling the multiple image-degrading effects (67).

## After therapy - Dosimetry

Post-treatment dosimetry for yttrium-90 microspheres is simplified compared to other forms of radionuclide therapy since the microspheres become lodged requiring only one time-point for imaging. For example, larger scale dose delivery assessment for the treatment plan can be performed on SPECT or PET images simply by estimating the activity ratio between tumor and parenchyma. As a bare minimum, this approach is reasonable since the correlation between MAA and microsphere distributions varies (68, 69, 70). To more accurately assess the absorbed dose to tumor and normal tissue a simple voxel-based method has been suggested. By assuming local energy deposition and adjusting the absorbed dose per decay (S value) to the size of the voxels (Eq. 8), only a calibration factor needs to be determined (71).

$$S_{Self\ dose} = \frac{\bar{E}^{\beta}_{90-Y}}{m_{voxel}} \qquad \text{Eq. 8}$$

Where the average beta energy for yttrium-90 is 933 keV (Table 1) and the mass of the voxel is determined by assuming a homogenous density. For the typical SPECT resolution of 4.42 mm cubic voxels and a density of 1.03 g/cm$^3$ the $S_{Self\ dose}$ = 1.669 Gy/GBq-s can be calculated.

To be effective, mean absorbed tumor doses over 100-120 Gy and 100 Gy have been proposed for HCC and mCRC, respectively, while, to be safe, the mean absorbed dose to the liver parenchyma should not exceed 40 Gy (72).

## Radiation-induced toxicity

Although a mean absorbed dose limit of 40 Gy to the liver parenchyma can be considered safe when treating a significant fraction of the liver volume with external beam radiation, a universally recognized absorbed dose threshold for RE with resin or glass microspheres has not been established. (73, 74). The threshold depends on the functional status of the liver and originates from external beam radionuclide therapy from where the absorbed dose cannot be directly translated due to the heterogeneous radiation field and low-dose rate in RE. For RE limited to a single lobe or segments higher mean absorbed doses to the liver parenchyma can be tolerated, partly due to the parallel structure of the liver lobules (74, 75).

Liver failure induced by irradiation of the liver parenchyma is potentially fatal and a major concern. A 2017 review concluded that radioembolization-induced liver disease (REILD) is not clearly defined but reported occurrences in 0-31% of treatments with an incidence of lethal outcome between 0-5% (76).

Lung shunt fractions exceeding 20% and tumor-to-normal tissue concentration ratios (TNC) below 2 are considered contraindications (60, 68). However, a retrospective study recently demonstrated no signs of radiation pneumonitis after RE in patients with HCC despite having lung shunt fractions over 20% (77). Tumor to normal tissue ratios can vary greatly between patients depending on tumor type, size and vascularization, from 7.2 (mean) for HCC in one study to 1.7 (mean) for mCRC in another (72).

## Somatostatin receptor-based radionuclide therapy

### Neuroendocrine tumors

For targeted radionuclide therapies the concept is to systemically deliver a radiopharmaceutical specifically to tumor cells throughout the body. Peptide receptor radionuclide therapy (PRRT), sometimes also referred to as targeted radionuclide therapy or molecular radionuclide therapy, targets specific receptors on tumor cells with a ligand coupled to an alpha or beta emitter. Somatostatin receptors (SSTR) belong to the G protein-coupled transmembrane receptors and exist in in five subtypes, SSTR1-SSTR5. SSTR are commonly expressed in a variety of tissues, such as the pancreas, spleen, liver and kidneys but it is mainly SSTR2 that is overexpressed and therefore targeted in many neuroendocrine tumors (78, 79). SSTR2 has also been identified in hematopoietic stem and progenitor cells with the highest expression on the $CD34^+$ and $CD117^+$ cells representing the most primitive subgroup (80, 81). Due to metabolic degradation naturally occurring somatostatin have a limited circulating half-life of a few minutes (82). Instead, more stable somatostatin analogs (SSAs) that bind to SSTR2 with high affinity have been developed (83). The SSA peptides octreotide, and later octreotate, have since demonstrated desirable biodistribution properties in tumors, with rapid accumulation and prolonged retention compared to other tissue types (84). By using a chelator, specifically dodecane tetraacetic acid (DOTA) in this case, with either of the peptides, DOTATOC (octreotide) or DOTATATE (octreotate) can be linked with yttrium-90, lutetium-177 or terbium-161. The importance of the combination of SSA and a radionuclide has been shown in-vitro through clearly increased tumoricidal properties for [$^{177}$Lu]Lu-DOTATATE compared to [$^{177}$Lu]Lu-DOTA (85). Retrospectively, multiple trials have been performed using [$^{90}$Y]Y-DOTATOC, [$^{90}$Y]Y-DOTATATE and [$^{177}$Lu]Lu-DOTATATE on patients with neuroendocrine tumors to determine treatment efficacy and safety. While the results were favorable in terms of progression-free survival and overall survival, an increased incidence of kidney toxicities, abdominal pain and other adverse effects were observed with yttrium-90, largely resulting in the replacement of yttrium-90 with lutetium-177 in recent years (86, 87, 88, 89, 90).

The first prospective randomized trial in patients with metastatic midgut NETs, NETTER-1, demonstrated increased progression-free survival and overall survival for [$^{177}$Lu]Lu-DOTATATE compared to high-dose SSA using a total of 4 administrations of 7.4 GBq [$^{177}$Lu]Lu-DOTATATE at an 8-week interval (91). In comparison to the control group, both the median progression-free survival and overall survival were longer at 28.4 and 48.0 months, compared to 8.4 and 36.3 months, respectively. This treatment regimen has been approved by the American and European medical agencies and is commercially available.

In comparison to the control group, the median progression-free survival was longer at 28.4 months compared to 8.4 months, and the overall survival was also longer at 48.0 months compared to 36.3 months.

### Patient selection

By applying the same peptide that is used for treatment, PET/CT imaging with gallium-68 ([$^{68}$Ga]Ga-DOTATATE) can be used for localization of tumors, disease staging and to select patients for PRRT (92, 93). The method has been shown to be accurate with high sensitivity and specificity compared to both previously used imaging methods such as $^{111}$In-DTPA-octreotide scintigraphy and pathology (94, 95, 96). The use of [$^{68}$Ga]Ga-DOTATATE PET/CT to predict therapeutic outcome or absorbed dose after treatment with [$^{177}$Lu]Lu-DOTATATE has been attempted but is not yet conclusive, i.e. observed correlations may not translate to the individual patient (97, 98). Dual-isotope PET/CT imaging has been proposed by also utilizing fluor-18 ([$^{18}$F]F-FDG PET/CT, a marker for glucose uptake correlated to the increased metabolism in tumor cells. By incorporating image data connected to both metabolism and SSTR density in the tumor classification, the study demonstrated significant correlations to overall survival in 62 patients (99). A recent study used blood samples and subsequent genomic analysis to select patients suitable for [$^{177}$Lu]Lu-DOTATATE treatments (100). The results are promising as the interim analysis demonstrated strong prediction accuracy in terms of identifying responders.

The combination of isotopes for both treatment and imaging is an interesting, although not new, prospect in quantitative imaging since identical chemical properties further simplifies conclusions between pre/post-therapy images, for example iodine-123 for imaging and iodine-131 for therapy and imaging in neuroendocrine tumors (101). Other feasible pairs have been proposed, such as the various isotopes of terbium. Terbium-152 (PET) or terbium-155 (SPECT) can be used for pre-treatment imaging, while terbium-161 (SPECT) or terbium-149 (PET) are theranostic isotopes that can be utilized for both therapy and imaging (102, 103, 104).

## Biodistributions

The retention (or elimination) of a radiopharmaceutical in a target region or its proximity will heavily influence the absorbed dose since slow elimination cause a greater number of decays and a larger time-integrated activity, Ã (Eq. 9).

$$\tilde{A}(r_s) = \int A(r_s, \tau) d\tau \qquad \text{Eq. 9}$$

The effective half-life, for a mono-exponential model, consists of both the physical half-life, a property of the radionuclide, and the biological half-life, determined by the region, patient-specific parameters such as glomerular filtration rate and receptor density, as well as the targeting agent or radionuclide (Eq. 10).

$$\frac{1}{t_{eff}} = \frac{1}{t_{phys}} + \frac{1}{t_{bio}} \qquad \text{Eq. 10}$$

Where, t is the half-life representing the rate (1/time) at which the effective, physical or biological decay occurs. For example, the disassociation of yttrium-90 from microspheres after radioembolization is typically far less than 0.1% of the injected activity. This means that microspheres, after any initial lung and gastrointestinal shunting, will be stationary and causes the effective half-life for the liver to approximately equal the physical half-life of the radionuclide (105). Contrarily for [$^{177}$Lu]Lu-DOTATATE treatments, the median effective half-life in the kidneys varies greatly from the biological half-life as well as between patients which was demonstrated in a 2020 study of 777 patients (106). Using a monoexponential fit and three SPECT/CT measurements, it was estimated that the median effective half-life for the kidneys is 52 hours. However, an early and late time point was found to be of particular significance in order to minimize extrapolations in the biodistribution, which may deviate and cause subsequent uncertainties in the absorbed dose estimates.

## Bone marrow dosimetry

Although the significance of the yellow marrow has been demonstrated in recent years, bone marrow dosimetry often aims at estimating the absorbed dose to the red marrow. Ideally, the estimated absorbed dose to the red marrow can be used to establish causal correlations to hematological toxicities and subsequently to minimize toxicities while maximizing therapeutic efficiency. However, this is no small task, as the limited resolution in SPECT images, the small volume of the bone marrow cavities, and the low activity concentrations make dosimetry for this region particularly challenging. Another challenge is the substantial prevalence of bone metastases in patients with neuroendocrine tumors leading to increased uptake from the tumors as well as

increased radiation exposure to remaining healthy bone marrow. Although image-based dosimetry can exclude skeletal sites with larger bone metastases, it's important to acknowledge that micrometastases and small tumors may evade detection in SPECT images.

An absorbed dose limit of 2 Gy for the bone marrow is generally applied in PRRT even though it has not yet been verified for recently developed therapies. The limit originates from iodine-131 treatments of metastatic thyroid carcinomas where the bone marrow is considered a main risk organ. In the original study from 1962, blood was used as a surrogate for red marrow and the absorbed dose was estimated using a scout-dose of iodine-131. The self-dose (to blood) was determined using blood samples and an absorbed fraction close to 1 while photon-irradiation from the remainder of the body was estimated with urine samples and probe measurements. No adverse hematological toxicities were observed in patients that received absorbed doses of 2 Gy or less to the blood compartment (107, 108).

In 1993, a blood-based dosimetry method for red marrow irradiation was proposed for radio-immunotherapy with antibodies (109). By assuming no specific uptake in blood cells, bone marrow, or trabecular and cortical bone and equal activity concentrations between the plasma and extracellular matrix in the bone marrow, a red marrow-to-blood ratio (RMBLR) between 0.2 and 0.6 was established, or 0.36 using baseline parameters (Eq. 11). The equation allows for individualization as the hematocrit (HCT) can be estimated from the blood samples and the red marrow extracellular fluid fraction (RMECFF) could be determined from biopsies or using MRI or CT-based methods. As long as the fundamental assumptions are valid, this approach can be extended to other radionuclide therapies.

$$\frac{Ac_{RM}}{Ac_{Blood}} = \frac{RMECFF}{1 - HCT} = RMBLR \qquad \text{Eq. 11}$$

Determining the activity concentration (AcBlood) in the blood at several time points is essential to establish the biodistribution. The main contribution to the absorbed dose to the red marrow is from the self-dose, which, for [$^{177}$Lu]Lu-DOTATATE, can be estimated from the activity concentrations in the blood samples by assuming that the activity concentration in the blood equals that of the red marrow, i.e., RMBLR = 1 (33, 110). By scaling the time-integrated activity concentration in the bone marrow with the bone marrow mass of the corresponding bone marrow compartment in the skeletal dosimetry model, the contribution from the self-dose to the absorbed red marrow dose can be estimated (Eq. 12).

$$\overline{D}_{RM \leftarrow RM} = \widetilde{Ac}_{Blood} \cdot RMBLR \cdot m_{RM,Phantom} \cdot S_{RM \leftarrow RM,Phantom} \qquad \text{Eq. 12}$$

The approach for image-based dosimetry is rather similar. Individual biodistributions are identified through sequential imaging with the first image usually around 4 hours after administration and then again after 24 and 168 hours to determine the elimination rate. The impact of imaging time-points has been studied, emphasizing that at least two imaging time points ensure accuracy and reproducibility one of which should be late (111, 112). As previously mentioned, the strength of the SPECT-based methods lies in the ability to directly quantify activity concentrations in the spongy bone rather than using the blood as a surrogate for the activity concentration in the bone marrow. In planar imaging, it is possible to distinguish between a high and a low uptake compartment through pixel-value thresholding (113). The high-uptake compartment includes regions with high SSTR2 density or physiological uptake, such as tumors, kidneys, the liver, and the spleen. If the uptake in bone marrow is assumed to be unspecific, its biodistribution can be associated with the low-uptake compartment. A single time point SPECT image at 24 hours after administration can then be used to quantify the activity concentration in the spongy bone (114). After determining the time-integrated activity, Ã, through curve-fitting and integration, the absorbed dose to the red marrow can be calculated using Eq. 5.

### Skeletal dosimetry models

Accurately determining the absorbed fractions and consequently S-values for bone marrow is difficult. Besides patient-specific variations of the red marrow distributions, detailed uptake beyond the resolution of the imaging systems is probably necessary.

Several skeletal models have been developed for beta emitting radionuclides attempting to add accuracy, consistency and transparency to the red marrow absorbed dose estimates. The most widely used models have resolved the marrow cavities in one of two ways. Initially, optically scanned trabecular bone samples from a 44-year-old man were measured to produce distributions that enabled sampling of electron path lengths through the cavities (115). This dataset has been used extensively and has been extended to other skeletal sites and used with MC radiation transport programs rather than with the original average range approximation (116). More recently image-based models have been developed, employing MRI or micro-CT on spongy bone biopsies to resolve the bone marrow cavities into 3D voxel matrices (117, 118, 119, 120). The discretization of images into voxels is necessary before they can be used as input for MC radiation transport programs. These image-based models have been expanded further to enable patient-specific adaptations in terms of red

and yellow marrow quantities and depth-dependent variations of hematopoietic stem cell distributions (121, 122). The effort of applying patient-specific parameters to dosimetry models has proven worthwhile as stronger dose-response correlations have been observed, as elaborated in the upcoming section (123, 124).

### Dose-response relationship

The ultimate objective of dosimetry is response prediction by correlating the absorbed dose to an outcome. However, due to the number of variables involved, it is necessary to increasingly strengthen correlations before prediction can be realized. The red marrow is particularly sensitive to ionizing radiation and it is therefore plausible to assume that the red marrow will be affected after [$^{177}$Lu]Lu-DOTATATE-treatments (125). To verify such a claim only blood samples are necessary since changes in platelet, hemoglobin or white blood cell counts would signify an affected red marrow. However, declining blood counts caused by irradiation need to be quantified to optimize treatments, both in terms of minimizing side effects and maximizing the amount of radiopharmaceutical. Embedded in the estimated absorbed dose to red marrow and the response data from blood sampling are the individual patient features such as radiosensitivity, biodistributions and baseline characteristics. A 2009 study correlated concentrations of [$^{177}$Lu]Lu-DOTATATE from blood samples with simultaneously collected bone marrow aspirates in 15 patients (110). The correlation was strong ($p<0.001$) with a linear regression correlation coefficient of 0.914, probably due to a significant fraction of blood in the bone marrow aspirate. However, the decreasing number of platelets after treatment could not be correlated to the red marrow absorbed dose estimated with the S value approach and a red marrow-to-blood activity concentration ratio equal to 1. This ratio was applied to the blood-based bone marrow dosimetry in a 2018 study of 200 patients that did not correlate absorbed dose estimates in the bone marrow to declining blood counts (126). Although no patient reached the 2 Gy absorbed dose limit 15% presented grade ¾ hematological toxicities.

A number of image-based studies, with both [$^{90}$Y]Y-DOTATOC and [$^{177}$Lu]Lu-DOTATATE have demonstrated correlations between the absorbed dose and decreasing platelets determined by blood sampling and have been suggested to more accurately estimate absorbed dose to the bone marrow than blood-based methods (127). Planar images were used in a 2016 study to separate low and high uptake compartments. The absorbed dose was estimated using the biodistributions of the low uptake compartment and correlated significantly ($p<0.01$) with decreasing counts of platelets, hemoglobin and white blood cells (113). The correlation with platelet decrease was strengthened ($p<0.0001$) in a subsequent study on another patient cohort by also utilizing a SPECT image at 24 hours after administration. Activity concentrations from spherical volumes of interest in the lumbar vertebrae were used to adjust the biodistribution from

the planar images (114). Three SPECT images were used in a 2019 study to demonstrate a weak but significant correlation ($p<0.01$) between platelet decline and the absorbed bone marrow dose in the L4 and L5 vertebrae (128). However, the absorbed dose estimate is subject to additional uncertainties since the last imaging time-point was only approximately 72 hours after administration. The strength of the correlations in these studies varies and is determined on a group level. So far, none are strong enough to be applied to individual patients with any certainty. However, gradual refinement of the methodologies involved has previously been proven to increase these correlations (127).

Furthermore, as the spleen receives high absorbed doses during [$^{177}$Lu]Lu-DOTATATE treatments and as a reserve for blood cells, the potential involvement of the spleen in hematological toxicities should perhaps not be surprising. Two image-based studies have significantly correlated spleen uptake, quantified through post-therapy imaging, to decreasing levels of hemoglobin (129, 130).

### Hematological toxicities

Systemic radionuclide therapy will inevitably irradiate the bone marrow to some extent and can cause significant adverse effects. Hematological toxicities are measured through blood sampling and are quantified by changes in the blood elements where grade 3 or 4 (NTC CTCAE) are considered serious (Table 4). Most patients experience hematological toxicities after [$^{177}$Lu]Lu-DOTATATE treatments but these are usually moderate and transient (131). Long-term toxicities are also a risk after PRRT, with leukemia and myelodysplastic syndrome occurring in 1-2% of patients (131, 132). Although the severity of hematological toxicities cannot yet be accurately predicted, several studies have correlated the absorbed dose to the bone marrow with a declining platelet count (113, 114, 128). Identified risk factors for developing serious hematological toxicities are age (> 70), treatment history, presence of bone metastases, initial bone marrow status and low creatinine clearance (131, 133). Increased frequency of hematological toxicities has been observed in patients also showing renal toxicity (134). In a 2013 study that involved 203 patients, a subgroup of 16 patients who had undergone splenectomy demonstrated a negative association with hematological toxicities, and none of grades 3 or 4 were developed (135).

***TABLE 4***

*Incidence of grade ¾ hematological toxicities after treatment of NETs with either or [$^{90}$Y]Y-DOTA-TOC or [$^{177}$Lu]Lu-DOTATATE. Cumulative administered activities are reported as the mean or median value of the total administered activity or, if not available, as the mean administered activity per cycle.*

| Author, year | PRRT | Number of patients | Grade ¾ hematological toxicity (%) | Cumulative administered activity (GBq) | Number of cycles (Median) |
|---|---|---|---|---|---|
| Imhof, 2011 | [$^{90}$Y]Y-DOTA-TOC | 1109 | 12.8 | 3.7/m$^2$ (Cycle) | 1-10 (2) |
| Bodei, 2015 | [$^{90}$Y]Y-DOTA-TOC | 358 | 14.2 | 10.1 (Median) | 1-11 (4) |
| Gupta, 2012 | [$^{177}$Lu]Lu-DOTATATE | 47 | 4.3 | 20.1 (Mean) | 2-6 |
| Bodei, 2015 | [$^{177}$Lu]Lu-DOTATATE | 278 | 3.1 | 22.9 (Median) | 1-10 (5) |
| Sabet, 2013 | [$^{177}$Lu]Lu-DOTATATE | 203 | 11.3 | 7.9 (Cycle) | (3) |
| Bergsma, 2016 | [$^{177}$Lu]Lu-DOTATATE | 320 | 11 | 29.6 (Median) | 4 |

## Small-scale dosimetry

The definition of small scale varies with the radionuclide, targeting principle and objective. Dosimetry for some therapies or organs can be straightforward, and the mean absorbed dose can suffice, as was the case for voxel dosimetry in normal tissue after radioembolization, where the long range of yttrium-90 beta particles have a flattening effect on the absorbed dose distribution to parallel lobules in the liver parenchyma (Fig. 11). Other therapies demonstrate heterogeneous absorbed dose distributions on scales that are much smaller than the system resolution or compared to the average range of beta particles. One such example is the significant emission of low-energy electrons from terbium-161 that may require sub-organ spatial dose distributions to sufficiently translate observed biological effects (136). A 2020 Monte Carlo study demonstrated stronger correlations for in-vitro cytotoxicity of human osteosarcoma cells irradiated by [$^{177}$Lu]Lu-DOTATATE for realistic cellular structures compared to the classically used spherical cells (137). The implications varied depending on where the activity was accumulated but indicate that lutetium-177 could be more effective than previous cellular models would suggest.

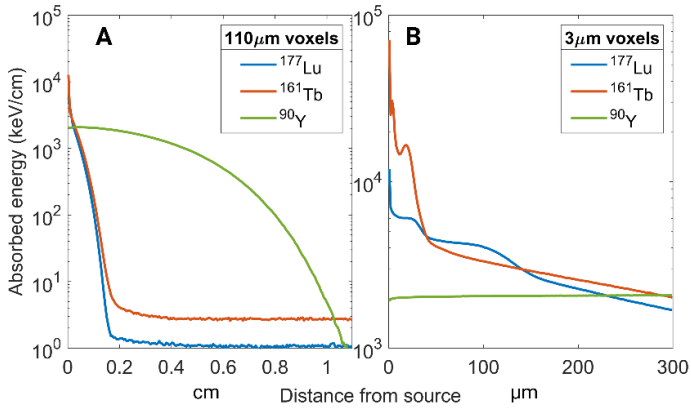


***FIGURE 11***. *Energy deposition from a point source with either lutetium-177, terbium-161 or yttrium-90 in two cubic voxel grids with sides of 110 µm (A) and 3 µm (B). Notice the logarithmic scales on the y-axes and the different distances on the x-axes.*

## Bone marrow quantification

An Australian group exploited the intense cellular proliferation in the bone marrow with 3-deoxy-3 [18F]-fluoro-L-fluorothymidine PET/CT to determine distributional variations of unaffected bone marrow in 51 cancer patients (138, 139). Although significant sex and age-related differences were seen, the results were fairly consistent with the standards used in bone marrow dosimetry models, for example showing the hip bones and thoracic and lumbar vertebrae as the largest reserves for red bone marrow. Unfortunately, patients eligible for radionuclide therapies cannot be assumed to have healthy or unaffected bone marrow. For example, two studies on NETs and GEP-NETs with 691 and 145 patients, respectively, found that 12-13% had skeletal metastases, although estimates vary between 4-13% depending on the primary tumor site (140, 141). The presence of skeletal metastases in a patient is relevant, not only for bone marrow dosimetry, due to its association with a worse prognosis (142). The uncertainty of pre-treatment bone marrow status is further indicated in another study where 58 of 91 patients treated with [$^{177}$ Lu]Lu-DOTATATE had hematological abnormalities at baseline (143).

Therefore, the amount of red marrow in patients with neuroendocrine tumors is highly individual and cannot be assumed a priori based on age and gender. In fact, studies demonstrate red marrow differences up to 50% in patients of similar gender and age (144, 145, 146). This is not surprising considering the bone marrow needs to be responsive to manage physiological stress. Furthermore, several studies utilizing magnetic resonance and healthy volunteers have demonstrated significant differences in marrow adipose tissue not only between groups of varying ages but also intra-patient vari-

ations between vertebrae. Trends of increasing marrow adipose tissue with age for men and women have been established, from 40-50% at 50 years to 65-75% above 80 years of age showing a particular increase for women between the ages of 55 and 65 (147, 148). Baum et al. demonstrated significantly increasing marrow adipose fractions when measuring from the $C_3$ to $L_5$ vertebrae, from 35-41% and 25-34% for males and females (n=28, 26±4 years), respectively, and these trends have been confirmed in other studies (149, 150, 151).

Histological analysis of the bone marrow status requires tissue samples, often collected from the hip bones or vertebrae (152). The potential improvement in dosimetric accuracy can hardly motivate this invasive procedure, which cannot be applied to multiple skeletal sites. Instead, image-based quantification of marrow adipose tissue can be used to quantify red marrow due to the inverse relationship between red and yellow marrow in the cavities of trabecular bone (Eq. 13). The cellularity of the bone marrow is defined as the proportion of red marrow, i.e. hematopoietically active cells, in the bone marrow.

$$Cellularity = 1 - \frac{V_{Adipose\ marrow}}{V_{Bone\ marrow}} \qquad \text{Eq. 13}$$

Where V represents the estimated volume of adipose marrow and bone marrow. Although the image-based procedures were largely developed for other purposes they may be applied to patient-specific bone marrow dosimetry. It should be noted, that the actual cellular composition of red marrow includes adipose marrow cells, although to a far lesser extent than in marrow adipose tissue (40% vs 95%) (153).

### Magnetic resonance

An attribute of magnetic resonance imaging (MRI) is the strong soft-tissue contrast which makes it useful for characterization of bone marrow tissues. While conventional MRI techniques such as $T_1$/$T_2$-weighted imaging could be used to separate red and yellow marrow, specialized methods have been applied to simplify interpretation and quantitation (154, 155). The proton density fat fraction (PDFF) is correlated to the concentration of fat (triglycerides) and therefore also to the concentration of marrow adipose tissue and is used as a reproducible and reliable biomarker (156, 157). PDFF is measured in one of two ways, either using chemical shift-encoded MRI or with single voxel proton magnetic resonance spectroscopy often considered the gold standard. Briefly, the hydrogen in fat and water have different precession frequencies, which can be exploited in chemical shift-encoded MRI by measuring inhomogeneities in the magnetic field and creating two separate images (158). Single voxel MRS pools the signal from a voxel of interest created by selectively exciting particular slices whilst

simultaneously spoiling unwanted signals from the outside (159). Both techniques provide high accuracy and robustness, producing a Pearson correlation coefficient of 0.979 when compared to determining marrow adipose content without increasing the patient's absorbed dose (160).

### Computed tomography

Compared to MRI, computed tomography (CT) examinations are more readily available, less time-consuming and less expensive. Furthermore, CT has short acquisition times, important to minimize motion-related errors, and excellent spatial resolution. However, the density in red marrow and yellow marrow only differs by 5% which makes the distinction between the two challenging (161). To quantify fat in relation to other tissue types, dual-energy CT has been suggested as it can utilize variations in the energy dependence of attenuation coefficients between materials. Several approaches can be used to create spectral separation of dual-energy CT, for example: two sequential measurements with varying energies on a regular CT system, an alternating x-ray tube current during a single measurement (low/high kV switching) or on a system with two source/detector sets (dual source CT) (162). Methods to quantify adipose marrow fat fraction is explored in multiple studies and excellent agreement has been demonstrated for the vertebral fat fraction when determined by dual energy-CT and MRI-based methods (146, 163, 164). A 2022 study of 83 patients determined an intraclass correlation coefficient of 0.918 when comparing dual-energy CT to MRI and estimating the vertebral fat fractions (165).

# AIMS

Although tumor dosimetry was involved in studies one and three, the common factor of the four studies included in this thesis is normal tissue dosimetry. The particular aims are best divided into treatment-based categories.

**Study I - Radioembolization**

The aim of Study I was to estimate the absorbed dose to tumor and normal tissue in a single patient using multiple imaging modalities with varying resolutions. From the pre-therapeutic injection of [$^{99m}$Tc]Tc-MAA and subsequent SPECT images to post-therapy bremsstrahlung SPECT and further to autoradiographic analysis of resected liver tissue and ultimately to the classification and gamma-well measurements of punch biopsies.

**Study II, III, IV - Bone marrow dosimetry**

Study II, III and IV all shared the aim of determining the absorbed dose to the red marrow. Additionally, each of these studies had specific aims, as outlined below.

Study II. Investigate how the absorbed dose to the red marrow in an established skeletal dosimetry model would be impacted by a shift from lutetium-177 to terbium-161 for radionuclide therapy.

Study III. Quantify potential uptake and retention in the spongy bone using a compartment model and determine the absorbed dose to the red marrow from SSTR2-based and blood-based irradiation after treatment with [$^{177}$Lu]Lu-DOTATATE.

Study IV. Develop a small-scale bone marrow dosimetry model for somatostatin receptor-based radionuclide therapies to estimate the absorbed dose to $CD34^+$ stem and progenitor cells irradiated by lutetium-177 or terbium-161.

# PATIENTS AND METHODS

Studies I and III, which involved patients, were conducted in compliance with the Helsinki Declaration and its subsequent amendments or equivalent ethical guidelines. Study I received approval from the regional ethics review board in Gothenburg, and Study III was approved by the Swedish Ethics Review Board.

## Radioembolization

A 63-year-old man was diagnosed with hepatocellular carcinoma at a single tumor site in the right liver lobe. Pre-study CT investigations revealed a tumor volume of 450 ml with 1050 and 500 ml of normal liver parenchyma in the right and left lobes, respectively. Showing no signs of cirrhosis in the liver parenchyma, radioembolization was selectively performed in the right lobe as a means to minimize the risk of recurring disease after tumor resection.

Before radioembolization, patient eligibility and procedure safety were investigated with both angiography and an injection of 150 MBq [$^{99m}$Tc]Tc-MAA. SPECT/CT images (Infinia Hawkeye, GE Healthcare) were collected with a high-resolution collimator (energy window: 126–154 keV). The images were used to estimate both the risk of extrahepatic shunting and the expected microsphere distribution in tumor and normal liver tissue, as well as the TNC.

Two weeks after the [$^{99m}$Tc]Tc-MAA injection, 2 GBq of yttrium-90 resin microspheres (approximately 40 million microspheres in 45 ml of saline solution) was selectively administrated to the right liver lobe via the right hepatic artery. An yttrium-90 bremsstrahlung SPECT/CT image was collected (energy window: 55-285 keV), Fig. 3C, using a medium energy collimator. Both pre- and post-therapy SPECT images were collected with 30 seconds per projection for a total of 120 projections and were reconstructed with an OSEM algorithm using CT-based attenuation correction. Reconstructions, delineations, and SPECT quantification were performed on the research group's imaging platform, PhONSAi.

Surgical resection was performed ten days after radioembolization, and the resected liver was fixated in isotonic formaldehyde for 48 hours, which enabled cleaving into 2 mm slices. 13–15 days after resection, the slices were placed between two autoradiographs (Amersham Hyperfilm MP, GE Healthcare) until a suitable level of exposure was reached. A total of 25 punch biopsies were taken from a central slice of the tumor. Each biopsy was weighed, put in a plastic vial filled with 10% formaldehyde, and measured using an automated gamma well counter (Wizard 1480, PerkinElmer). For mi-

croscopic analysis of the biopsies 8 µm sections were mounted on glass slides and stained with hematoxylin and eosin. The biopsies were randomized and analyzed by a pathologist.

### Dosimetry

As no signs of excessive shunting were observed and a measurement of the microsphere vial showed an insignificant amount of activity remaining, the bremsstrahlung SPECT dosimetry was performed by assuming that all microspheres remained in the liver (Eq. 14). The tumor and normal liver parenchyma were delineated using the CT, and the same VOIs were used for the [$^{99m}$Tc]Tc-MAA and 90Y-bremsstrahlung SPECT to determine the TNC.

$$\overline{D} = \frac{A_{Tumor}}{m_{Tumor}} 50 \left(\frac{J}{GBq}\right) \qquad \text{Eq. 14}$$

Where the mean absorbed dose D to the tumor is estimated using the activity in GBq and tumor mass from the VOI.

The absorbed dose to the biopsies was estimated using their measured weight and the gamma well counters detection efficiency originating from a calibration with yttrium-90 of 0.185 counts/decay. The exposure in the autoradiographs was fitted to the absorbed dose from the biopsies using a common logarithm in MATLAB (MathWorks). To manage saturation effects caused by overexposure, a dose of 200 Gy was assigned to all normalized pixels with values above 0.882.

## Somatostatin receptor-based radionuclide therapy

### Patients and imaging

For Study III, a total of 17 individuals were evaluated. They had been diagnosed with gastroenteropancreatic neuroendocrine neoplasms and underwent treatment with [$^{177}$Lu]Lu-DOTATATE (Lutathera, AAA). The patients, with a median age of 77 years, ranging from 58 to 88 years, received 7.4 GBq/cycle at intervals of 6-8 weeks. Prior to treatment, pre-therapeutic [$^{68}$Ga]Ga-DOTATATE PET/CT scans revealed that seven of the patients had bone metastases. After the initial treatment cycle, four SPECT images were obtained at 4, 24, 48, and 168 hours after administration using an energy window of 208.4 keV ± 10% with scattering windows surrounding the emission window at 187.5 keV -5% and 229.2 keV +5%, respectively. These images were then reconstructed with 6 iterations and 10 subsets using an MC-based OSEM algorithm to correct for attenuation and scatter effects as well as collimator-detector response (30).

### Bone marrow dosimetry

A Florida-based group has conducted research on bone marrow dosimetry for decades, which has yielded several significant publications (118, 120, 121, 122, 166, 167, 168). To varying degrees, their work has been utilized in all three bone marrow studies within this thesis.

Currently, three clinical trials are recruiting patients for peptide receptor radiotherapies with terbium-161 (clinicaltrials.gov). One of these studies focuses on somatostatin receptor-based targeting of NETs. While Study I employed pre-existing skeletal dosimetry models for both male and female subjects, Study IV modeled individual bone marrow stem cells to investigate the potential effects of terbium-161 on the bone marrow. Study IV was motivated by the additional 11.1 electrons with energies below 10 keV that are emitted with every terbium-161 beta decay (Table 1). These electrons have an average range of 3 µm, far below the resolution of the skeletal dosimetry model used in Studies II and III (50 µm).

## Study II

Specific absorbed fractions (SAF) have been published for monoenergetic electrons irradiating red marrow (referred to as active marrow in the models) for the University of Florida Adult Male/Female (UFHADM and UFHADF) skeletal dosimetry models used in Study II and III (Eq. 15) (120, 168). The original studies and their respective supplements contain all the phantom-specific parameters used in the following calculations. The microstructure of the bone marrow in these models, originating from micro-CT, is resolved with cubic voxels with sides of 50 µm and by applying decay data from ICRP 107 and linear interpolation, this enables the deduction of radionuclide specific S-values (Eq. 16) (16).

$$\mathrm{SAF}(\mathrm{RM} \leftarrow r_s, E_i) = \frac{AF(\mathrm{RM} \leftarrow r_s, E_i)}{m_{RM}} \qquad \text{Eq. 15}$$

Where AF is the absorbed fraction of energy in the red marrow (RM), the target region of mass m is irradiated by electrons of energy i from the source region rs.

Although the overall aim was to investigate terbium-161, lutetium-177 was included as a chemically related and currently relevant alternative to terbium-161. Yttrium-90 was selected for its characteristics as a high-energy beta emitter and extensive history of clinical use. The radionuclides irradiated the red marrow from one of four separate regions: the red marrow (RM ← RM), i.e., self-dose, yellow marrow (RM ← IM), or homogeneously distributed on the surface (RM ← TBS) or throughout the volume

(RM ← TBV) of trabecular bone. Although the shallow marrow, considered a surrogate region for bone-forming osteoprogenitor cells associated with bone cancer, is modeled in the UFHADM and UFHADF, it was not included in our analysis.

As the red marrow distribution and composition vary between skeletal sites, thirteen skeletal site-specific S values were calculated for each of the radionuclides and each of the four source regions (Eq. 16).

$$S_x(\mathrm{RM} \leftarrow r_s) = \sum_i E_i Y_i \, SAF_x(\mathrm{RM} \leftarrow r_s, E_i) \qquad \text{Eq. 16}$$

Where the S value for skeletal site x is the sum of all nuclear transitions i and their respective energy $E_i$ and yield $Y_i$.

The absorbed dose to the bone marrow is usually not reported for individual skeletal sites in dosimetry studies. Instead, an averaging of the S-values is performed so that a single S value can be used to represent the entire skeleton (Eq. 17) (118).

$$S_{Skeletal\ average}(\mathrm{RM} \leftarrow r_s) = \sum_x \frac{m_{RM,x}}{m_{RM,Tot}} \frac{m_{s,x}}{m_{s,Tot}} S_x(\mathrm{RM} \leftarrow r_s) \qquad \text{Eq. 17}$$

Where m denotes the mass of the red marrow or source region for either a single skeletal site x or the corresponding total mass for all skeletal sites. The process of calculating the average was then carried out again for the four source positions to calculate the S value for the spongy bone (SB) (Eq. 18).

$$\mathrm{S}(\mathrm{SB} \leftarrow \mathrm{SB}) = \sum_s \frac{m_{s,Tot}}{m_{SB,Tot}} S_s(\mathrm{RM} \leftarrow r_s) \qquad \text{Eq. 18}$$

This was motivated by the relatively poor resolution of SPECT images compared to the microscopic and potentially heterogeneous distribution of activity throughout the spongy bone. To further emphasize the impact of the varying resolutions, the energy deposition from the three radionuclides was simulated using PENELOPE (17). The cubic voxels in the simulations were sized according to the average diameter of a hematopoietic stem cell, 8.2 µm (169). Fig. 12 displays a visual comparison between the voxel scales of SPECT (4.42 mm), UFHADM/UFHADF (50 µm), and CD34+ hematopoietic stem cells (8.2 µm).

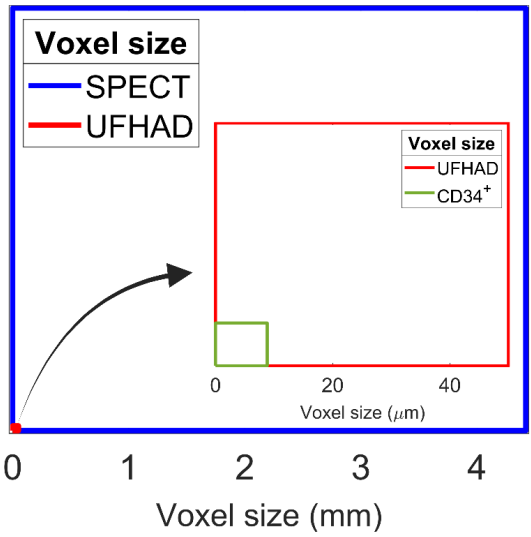


***FIGURE 12**. A relational visualization of the voxel sizes involved in bone marrow dosimetry from the 4.42 mm SPECT voxels (blue) to the 50 m voxels of the skeletal models (red) and the suggested voxel size necessary to resolve a single hematopoietic stem cell (green). The red square in the left hand corner is enlarged to show the green square. Created with BioRender.com.*

## Study III

$CD34^+$ hematopoietic stem cells were shown to express SSTR2 in a 2002 study (81). This is noteworthy considering it is also the molecular target for tumors in SSTR-based radionuclide therapies. The four consecutive SPECT images collected after the first treatment cycle were used to analyze the SSTR2-related uptake in the red marrow.

### Compartment model

To obtain as much data from the spongy bone as possible from each patient that was also consistent between patients, we identified and delineated 12 potential skeletal sites in the CT images (Fig. 13). Nine of the skeletal locations were identified in the spine, ranging from the ninth thoracic vertebra to the fifth lumbar vertebra. Accompanying these were the lower segment of the sternum bone and the left and right ilium segments of the hip bones. Further, the descending aorta was identified as a compartment containing pure blood, while subcutaneous adipose tissue was delineated as a compartment without any distinct uptake characteristics. Lastly, to represent a compartment with a notable presence of SSTR2, a tumor was identified and delineated in each of the ten patients without bone metastases. Data were extracted from each delineated region, and voxel values were translated to activity concentrations using a

phantom measurement with lutetium-177 of known activity and volume. In order to achieve a higher level of accuracy in the representation of the vertebrae and hip bones, the activity concentrations of all individual vertebrae as well as the left and right hip bones were combined and treated as single skeletal sites. The sternum was later excluded from the analysis as it posed difficulties in delineation and resulted in insufficient data.

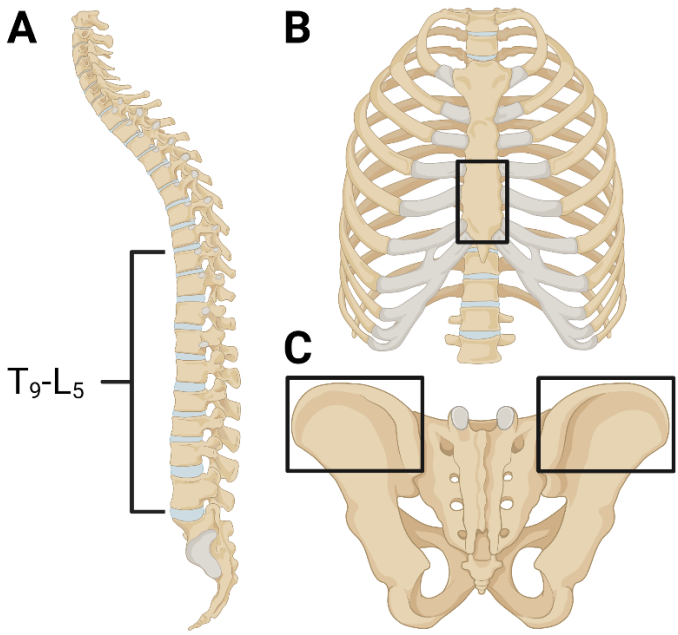


***FIGURE 13**. Positions of the twelve skeletal sites that were delineated in Study II. The nine vertebrae ($T_9$-$L_5$) (A), the sternum bone (B) and the left and right ilium bone (C). Created with BioRender.com.*

A pharmacokinetic compartment model was utilized by assuming that the activity concentration in a skeletal site consists of two components: blood-based activity and activity potentially related to a specific uptake on cells expressing SSTR2, either $CD34^+$ stem and progenitor cells. The biodistribution was estimated for the blood-based activity concentration with a bi-exponential function using the thoracic aorta (Eq. 19). Using the compartment model, the contribution of blood was eliminated from the spongy bone or tumor compartments to estimate the biodistribution resulting from specific uptake (Eq. 20).

$$C_{Blood}(t) = A_1 e^{-\lambda_1 t} + A_2 e^{-\lambda_2 t} \quad \text{Eq. 19}$$

Where t is the time after administration, and the curve fit parameters A and λ were optimized using MATLAB (MathWorks).

$$\frac{dC_{Specific}(t)}{dt} = k_1 \cdot f \cdot C_{Blood}(t) - k_2 \cdot C_{Specific}(t) \quad \text{Eq. 20}$$

The compartment model parameters k1, k2, are constants controlling the flow of activity into and out of the specific uptake compartment ($C_{Specific}$), while f modifies the blood concentration to match the nonspecific binding concentration ($C_{Nonspecific}$) derived for the plasma volume distribution in the bone marrow.

## Dosimetry

To calculate the absorbed dose to the red marrow, two methods were employed. The first method determined the absorbed dose estimate based on specific and nonspecific uptake and skeletal site-specific S values (Eq. 21).

$$D_{RM,x} = \left( \sum_t \frac{C_{Specific,x}(t)}{f_{RM,x}} V_{RM,x} + \sum_t \frac{C_{Specific,x}(t)}{f_{RM,x}} V_{RM,x} \right) S_x(RM \leftarrow RM) \quad \text{Eq. 21}$$

The second method utilized skeletal averaged S values and relied entirely on blood-based measurements, equating the activity concentration in the bone marrow with that measured in the aorta (Eq. 22).

$$D^{Blood-based}_{RM,Skeletal\ average} = \left( \sum_t \frac{C_{blood}(t)}{f_{RM}} V_{RM} \right) S_{Skeletal\ average}(RM \leftarrow RM) \quad \text{Eq. 22}$$

S values for lutetium-177 for the lumbar and thoracic vertebrae, the os coxae (hip bones), and the skeletal average from Study II were used along with the corresponding volume ($V_{RM,x}$) and volume fractions ($f_{rm,x}$) related to the UFHADM and UFHADF phantoms used. The time-integrated activities for the corresponding compartments can be found within the parentheses of Eq. 21 and Eq. 22. No tumor dosimetry was performed.

## Study IV

As hematopoiesis is mainly maintained by $CD34^+$ cells, these were the focus of the bone marrow model (38). The building of the bone marrow model was initiated by choosing spherical cell parameters. Two cell types were modeled: yellow marrow (radii 30 ± 2 µm) and red marrow (4.1 ± 1 µm) (169, 170). The rejection method was used to randomly label 2% of the red marrow cells as $CD34^+$ (171). To limit the number of bodies in the model, no cell nucleus was included. The size of the model was determined by the mean electron range of terbium-161 in soft tissue, approximately 300 µm (Fig. 2), and the distribution of $CD34^+$ cells. In 2006 and 2009, two studies were conducted to measure the distribution of CD34+ stem and progenitor cells in biopsies from the vertebrae, iliac crest, and ribs (166, 167). The studies found that the concentration of these cells decreased as the distance from the trabecular bone increased. Bone marrow samples in the $L_1$ vertebrae demonstrated no cells beyond 700 µm measured from the trabecular bone surface. A box with sides measuring 700 µm was created, and three of these boxes were arranged side by side. Trabecular bone of 50 µm thickness was then inserted between the boxes, as depicted in Fig. 14. A central block measuring 100x100x700 µm was chosen as a boundary for radiation equilibrium, and only $CD34^+$ cells inside were used to tally the energy deposition.

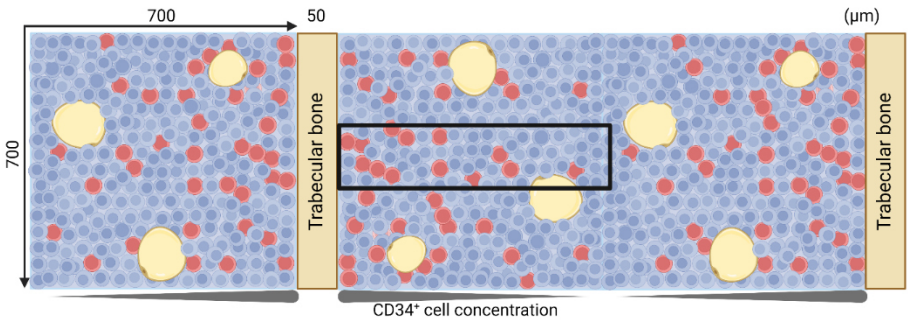


***FIGURE 14**. A visualization of a bone marrow model (not drawn to scale) $CD34^+$ stem and progenitor cells are represented by red cells, distributed along negative gradients emanating from the surfaces of trabecular bone (grey tapered lines). The blue and yellow cells denote red marrow cells and adipose marrow, respectively. The central black box indicates the area where the energy deposition in $CD34^+$ cells is calculated. Created with BioRender.com.*

Next, we utilized an open-source random sphere packing algorithm to fill the boxes with randomly sampled spheres of the corresponding dimensions (172). Aimed at packing metal powder, the algorithm did not find the optimal close-packing but rather a pre-defined packing density, which was set to 0.55. In order to replicate the distribu-

tion of CD34+ cell density sampled from the $L_1$ vertebrae, the bone marrow cellularity, i.e., the proportion of hematopoietic cells in the volume, was fixed at 70%.

Using MATLAB (MathWorks), the bone marrow model was transformed into several input files to facilitate simulations with PENELOPE. The following values were assigned to the simulation parameters for both terbium-161 and lutetium-177: $E_{abs} = 10^3$, $C_1 = 0.05$, $C_2 = 0.05$, $W_{CC} = 10^3$, and $W_{CR} = 10^3$. All $CD34^+$ cells were assigned activity, but only the centrally located ones were used to tally the deposited energy (Fig. 2). Irradiation from nonspecific uptake in the extracellular matrix was accounted for by homogenously distributed activity in between cells. Self-dose to the nucleus (N) was calculated in a separate simulation where a single cell consisting of a nucleus (r = 1.85 µm) with a surrounding cytoplasm was modeled. Activity in the single cell model (SCM) was placed either homogenously in the cell (C), in the cytoplasm (Cy), or on the cell surface (Cs) and used to adjust the simulation results from the bone marrow model (BMM) (Eq. 23).

$$Edep^{BMM}_{Corrected} = Edep^{BMM} - Edep^{SCM}_{C \rightarrow C} + \left(Edep^{SCM}_{Cy \rightarrow N} \; or \; Edep^{SCM}_{Cs \rightarrow N}\right) \quad \text{Eq. 23}$$

In order to make the bone marrow model more versatile, such as for image-based dosimetry, scaling of the activity concentrations obtained from SPECT images is required (Eq. 24).

$$Ac_{CD34^+} = \frac{Ac_{Spongy\ bone}}{Vf_{Bone\ marrow}\ Cellularity\ Vf_{CD34^+}} \quad \text{Eq. 24}$$

Equivalently, the scaling can be utilized for activity concentrations in blood (Eq. 25).

$$Ac_{ECV} = \frac{Ac_{Aorta}}{(1 - Packing\ density)\ Vf_{Plasma}} \quad \text{Eq. 25}$$

These computations facilitate the estimation of the absorbed dose for CD34+ cells, in this case obtained using parameters in Table 5 (Eq. 26).

$$D^{CD34^+}_{Specific\ uptake} = \frac{Ac_{CD34^+} Edep^{BMM}_{Corrected}\ V_{L-vertebrae}}{m_{L-vertebrae}} \quad \text{Eq. 26}$$

***TABLE 5***

*Parameters employed in the absorbed dose estimations.*

| Scaling parameters | % |
|---|---|
| * $Vf_{Bone\ marrow}$ | 87.4 |
| $Vf_{CD34^+}$ | 2 |
| $Vf_{Plasma}$ | 45 |
| * Cellularity | 70 |
| Packing density | 55 |

* Lumbar vertebrae from the UFHADF

# RESULTS AND DISCUSSION

## Study I

By pure visual inspection, the conformity between the [$^{99m}$Tc]Tc-MAA and the $^{90}$Y-bremsstrahlung SPECT was poor, if not completely absent (Fig. 15). This is supported by the discrepancy in the distribution of voxel values gathered using the same VOI for both images. Although a topic of some debate, a 2021 study deemed pre-therapeutic SPECT as effective for estimating the absorbed dose in normal tissue but ineffective when applied to tumor dosimetry. The reason for this could be attributed to variations in particle properties between MAA and resin microspheres, mismatch in catheter injection positions during simulation and treatment, and misalignment between [$^{99m}$Tc]Tc-MAA SPECT and $^{90}$Y-PET acquisitions. (173).

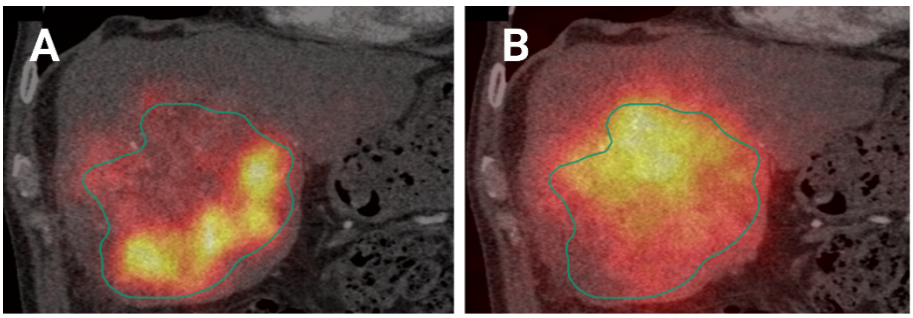


***FIGURE 15**. Coronal SPECT images of the liver demonstrating uptake in the delineated tumor VOI (green line) in the pre-therapeutic [$^{99m}$Tc]Tc-MAA image (A) and the post-therapeutic distribution of $^{90}$Y microspheres (B).*

Unsurprisingly, the mean absorbed dose to the tumor was comparatively low compared to the other estimates, determined to be 73 Gy using the SPECT images, but it is visually clear that the local variations within the tumor were large (Fig. 15B). This could be because the microspheres predominantly cluster in regions with viable tumor tissue, as was demonstrated in the biopsy analysis, or due to the catheter injection position. Although the reported absorbed dose to tumors is wide for RE with resin microspheres, 73 Gy would be considered a relatively low mean tumor dose. Particularly since, for 120 patients with HCC, a mean absorbed tumor dose over 100 Gy, determined by [$^{99m}$Tc]Tc-MAA dosimetry, was correlated to longer overall survival (174). For ablative purposes prior to resection or transplantation, a mean absorbed dose exceeding 400 Gy has been associated with complete tumor necrosis using glass micro-

spheres (175). However, the accuracy of the delineation of the tumor VOIs could be questioned as no arterial phase CT was available to simplify the segmentation. The continuous nature of the bremsstrahlung photons have a smoothing effect on the SPECT image, as illustrated by the moderate coefficient of variation (CV) from the tumor VOI, 0.35 compared to 0.59 for the [$^{99m}$Tc]Tc-MAA SPECT image.

The level of heterogeneity within the tumor is best shown using autoradiography, and the methodology could be used for future measurements if similar exposure times and activity concentrations could be ensured. While the response is roughly linear for intermediate exposure, obtaining appropriate levels of exposure is most challenging when dealing with low or high activity concentrations. The calibration curve obtained using the logarithmic curve fit was not forced through the origin (Fig. 16). While this provided a satisfactory fit to the biopsy data overall, pixels with values close to zero were given an arbitrary absorbed dose. To avoid overestimating the absorbed tumor dose, the image saturation observed in regions with high activity concentrations was managed by implementing a 200 Gy threshold.

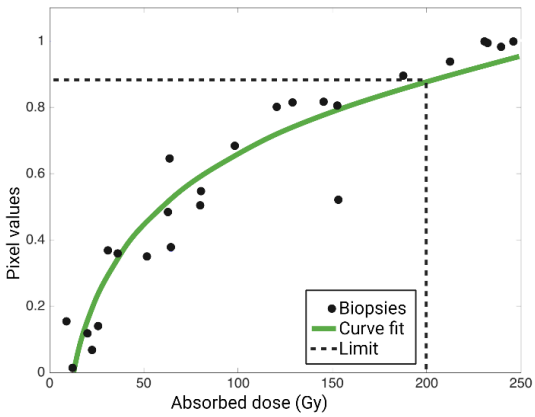


***FIGURE 16**. A logarithmic curve fit was employed to calibrate the absorbed dose estimates in the autoradiograph. The absorbed dose and mean pixel value for each biopsy are denoted by the black dots. The dashed line indicates the threshold dose, where all pixel values exceeding 0.86 are assigned the same absorbed dose of 200 Gy.*

A visual examination of the autoradiograph revealed three distinct regions (Fig. 17B). Tumor regions with intense labelling, intermediately labelled regions exhibiting both individual microspheres and significant clustering, and unlabeled regions without microspheres or cross-irradiation. The TNC was determined to be 6.4, and the absorbed

dose to the tumor and normal tissue was determined to be 109 and 17 Gy, respectively, with a CV of 0.27 and 0.10.

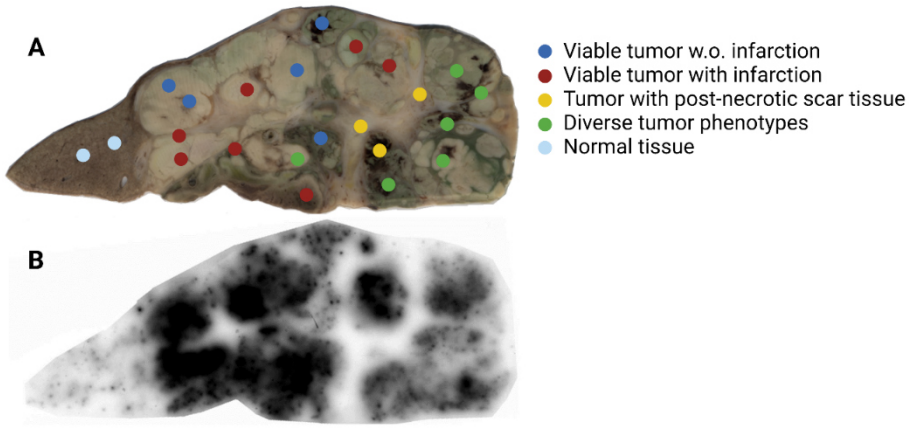


***FIGURE 17**. A central slice of the tumor and the corresponding punch biopsies (A). An autoradiograph of the same tumor slice (B). Created with BioRender.com.*

Five distinct tissue morphologies could be identified in the 23 analyzed biopsies: liver parenchyma, viable tumor tissue with and without infarction regions, and post-necrotic scar tissue (Fig. 17A). Although widely ranging throughout the tumor, high absorbed doses were almost only observed in tumor tissue classified as viable (Fig. 18). The necrotic biopsies probably have a compromised arterial perfusion, which could explain the lower absorbed dose. Another reason for the observed microsphere heterogeneities is the formation of clusters. As has been previously demonstrated, microsphere clustering will negatively impact the flow of microspheres below the cluster, preventing microspheres from reaching arterioles (176). Of the 12 viable tumor biopsies, one stands out at only 9 Gy. When removed, the mean absorbed dose estimate to viable tumor is 160 Gy, with a CV of 0.43. In one of the biopsies classified with diverse tumor phenotypes, the necrotic area was surrounded by viable tumor, and this biopsy also stands out with 231 Gy compared to the mean of 48 Gy (CV = 0.55) for the eight other non-viable tumor biopsies. Although only two biopsies were punched from normal tissue, with a mean absorbed dose of 23.5 Gy, the low CV of 0.10 for this region suggests more evenly distributed microspheres, and this observation is confirmed by the autoradiography. The autoradiograph and biopsy measurements support the concept of a highly selective treatment primarily targeting viable tumor tissue.

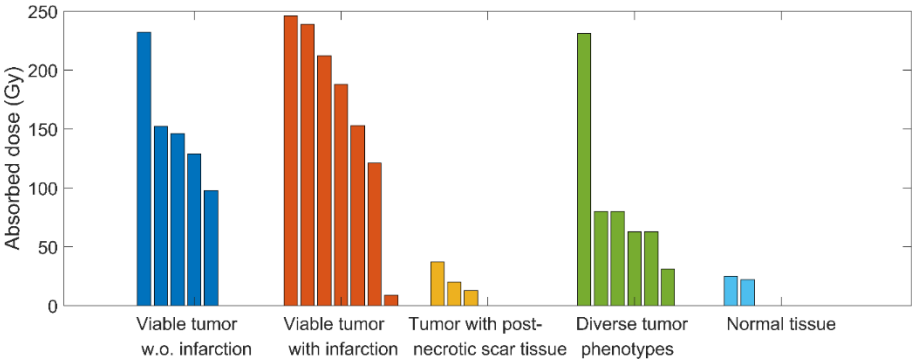


***FIGURE 18**. Classification of 23 biopsies and their corresponding absorbed dose measured in a gamma well counter.*

## Study II

Preemptively, it is reasonable to assume that the bone marrow exposure will increase significantly for terbium-161 if compared to lutetium-177 since 15% more energy is released per decay. However, for low-energy electron emitters, there are sharp gradients in the energy deposition, which can potentially have both sparing and hazardous effects in terms of irradiating critical structures (Fig. 20A). Although increased S values were calculated for terbium-161 compared to lutetium-177 for particular skeletal sites and source distributions, they were not demonstrated across-the-board, indicating the importance of accurate determination of microscopic activity distributions (Fig. 19A).

A number of studies, described below, have demonstrated favorable antitumor effects for terbium-161, most often compared to lutetium-177. Theoretical studies have used Monte Carlo-based methods to focus on the highly localized energy deposition in single cells and small tumors. For single cells with an equal energy density (1 MeV/$\mu m^3$), terbium-161 was shown to deliver a higher absorbed dose to the cell nucleus compared to lutetium-177 (177). The absorbed dose increased between 2.6 and 4 times for terbium-161, depending on the cellular activity distribution. Several other theoretical studies have demonstrated equally promising results for terbium-161 in small tumors and multiple metastases, attributing approximately 71% of the absorbed dose to Auger and conversion electrons (178, 179, 180, 181).

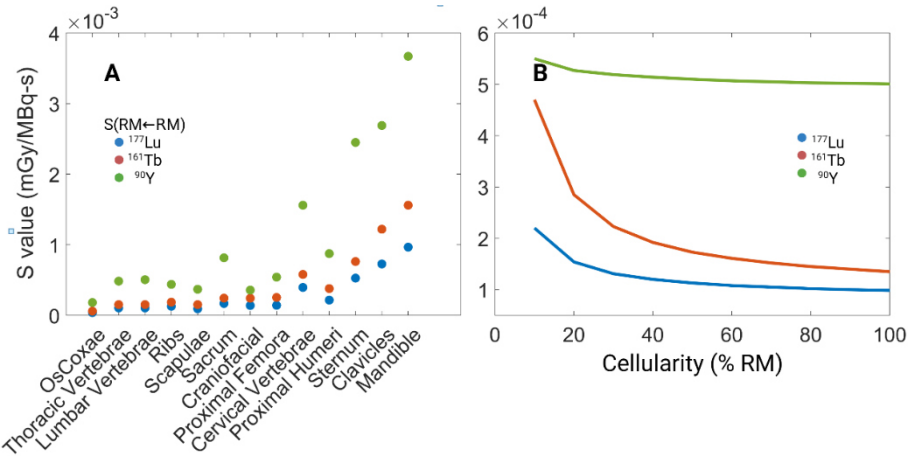


***FIGURE 19**. S values for red marrow self-irradiation in 13 skeletal sites of the male UFHAD (A). S value dependence on bone marrow cellularity variations for the three radionuclides (B).*

The largest differences in S values between terbium-161 and lutetium-177 were seen for self-irradiation at skeletal sites with a small proportion of the total RM (Fig. 19A). With fewer RM voxels or as the distance between them increases, the cross-dose between RM voxels decreases. These effects were also evident when calculating S values with decreasing bone marrow cellularity, with the discrepancy between the S values for terbium-161 and lutetium-171 increasing as the bone marrow cellularity decreased (Fig. 19B). Considering the relatively high mean age of patients receiving [$^{177}$Lu]Lu-DOTATATE as well as prior treatment history, deviations from the reference bone marrow cellularities are bound to be common. Results such as these can potentially add insight to the hematological toxicities observed in patients with an absorbed dose to the red marrow well below the 2 Gy threshold. For yttrium-90, similar trends were not observed, which is explained by the fact that the long-range beta particles counteract the increased distances between RM voxels. The same rationale explains why yttrium-90 had the highest S values of the three radionuclides, irrespective of source distribution or skeletal site. Fig. 20 shows that in smaller voxels of sizes similar to hematopoietic stem cells (Fig. 12), the precise localization of energy deposition from terbium-161 and lutetium-177 is more clearly illustrated. Although it may be essential to comprehensively elucidate hematological toxicities following Lu-DOTATATE treatments, accurately determining activity distributions on a microscopic scale may not be feasible.

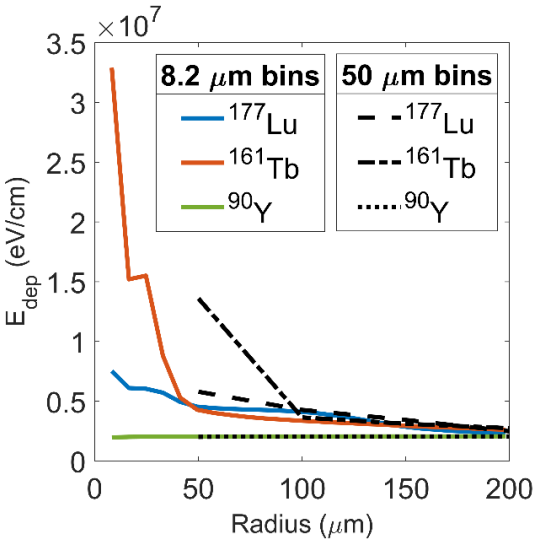


***FIGURE 20**. Energy deposition in two voxel grids for the three radionuclides in Study II. The colored lines represent a grid of voxels with 8.2 µm sides and the black dashed lines show the corresponding energy deposition in a 50 µm voxel grid.*

Clinical studies have demonstrated increased rates of grade ¾ hematological toxicities (CTCAE v.4.0) in patients treated with [$^{90}$Y]Y-DOTATOC (14.1%, n = 360) compared to those treated with [$^{177}$Lu]Lu-DOTATATE (3.1%, n=290) (182). Hematological toxicities were observed irrespective of equal or sometimes lower absorbed bone marrow dose estimates for yttrium-90. However, the 2014 analysis only included blood-based dosimetry on a small fraction of the patients, suggesting improved models and dosimetry methods are necessary.

## Study III

Using the SPECT images, a longer retention was consistently observed in the biodistributions from the spongy bone compared to the blood and subcutaneous adipose tissue for the seventeen patients and skeletal sites, which was attributed to specific uptake in the red marrow. The activity retention in the subcutaneous adipose tissue was found to be comparable to that observed in the blood. The seven patients with confirmed bone metastases had increased uptake in the spongy bone compared to patients with no bone metastases (Fig. 21). Rather than estimating the absorbed dose to all skeletal sites, the $T_9$-$L_5$ vertebrae and left and right hip bones were averaged (Fig. 22).

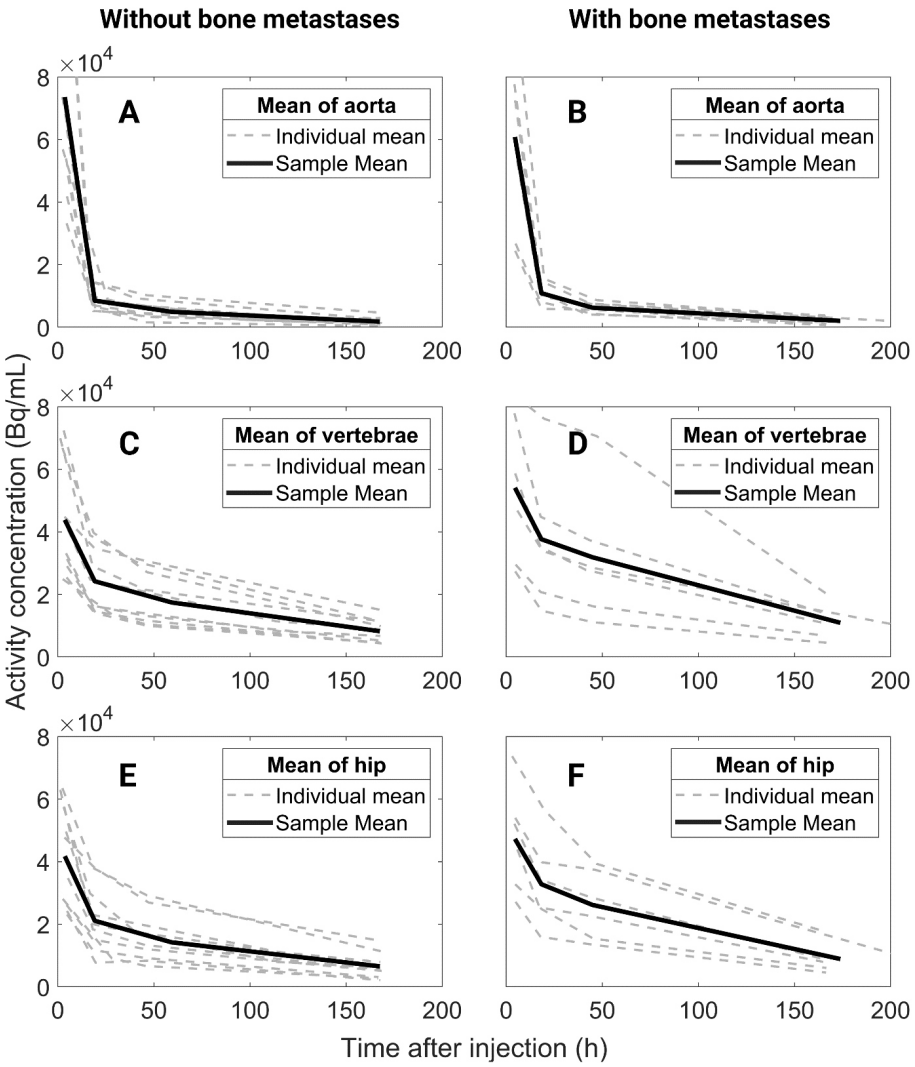


***FIGURE 21***. *Activity concentrations from the blood (A,B) and the spongy bone of the vertebrae (C,D) and hip bones (E,F) The figures in the left-side column include ten patients without bone metastases, and the right-side column includes seven patients with bone metastases. Gray dotted and black solid lines represent the individual patient mean and the mean of all patients in the sample, respectively.*

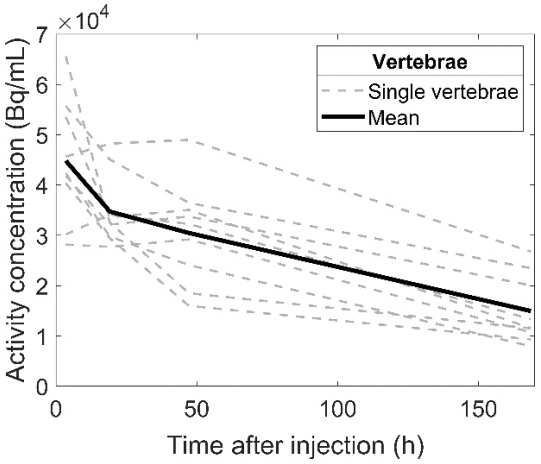


***FIGURE 22**. Activity concentrations for each of the delineated vertebrae ($T_9$-$L_5$) in a single patient (dashed) and the corresponding mean of all vertebrae (solid).*

Higher uptake was observed in the vertebrae compared to the hip bones, potentially due to the higher concentrations of $CD34^+$ cells in the vertebrae, as the reference bone marrow cellularity of the vertebrae is 70% compared to 48% for the hip bones (183). Although these results are already interesting in terms of consequences for red marrow dosimetry, a compartment model was used to separate the fast clearance of lutetium-177 in the blood from the slow release in the red marrow. In addition to a better comprehension of the activity distribution inside bone cavities, this separation allows for separate scaling of the specific and nonspecific contributions to the absorbed red marrow dose, which can potentially increase the accuracy of the dosimetry estimates. According to the biodistributions from the compartment model, specific uptake was the dominant contributor to the absorbed dose in the red marrow (Fig. 23). These results deviate from the rationale in the 2022 EANM dosimetry guidelines for $^{177}$Lu-labeled PRRT, namely that most of the radiation exposure to the red marrow stems from circulating radiopharmaceuticals (36).

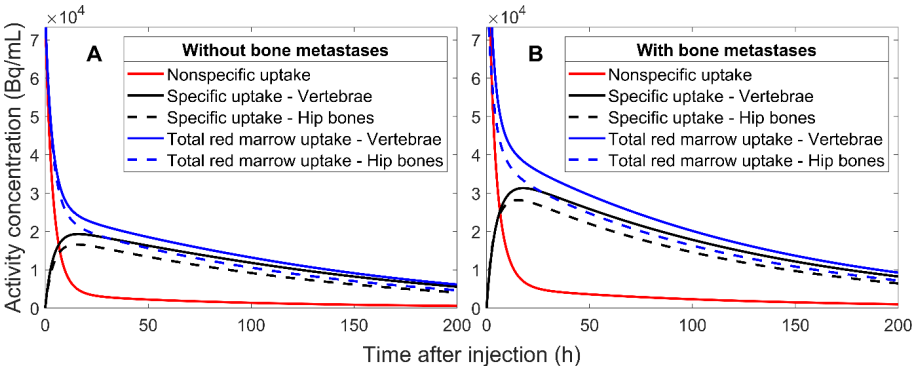


***FIGURE 23**. Results from the compartment model are presented as the mean of all patients for patients without (A) and with bone metastases (B). Red, black, and blue lines represent the blood, specific uptake, and total uptake, respectively, for the vertebrae (solid) and hip bones (dashed).*

In patients without bone metastases, the median absorbed dose estimates (median ± SD) from specific and nonspecific uptake in the vertebrae and hip bones were 0.056 ± 0.023 and 0.043 ± 0.022 Gy/GBq, respectively. This corresponds to the absorbed dose estimates for red marrow of 0.049 ± 0.026 Gy/GBq averaged from eight studies where image-based dosimetry was also applied (114, 128, 184, 185, 186, 187, 188, 189). The specific uptake accounted for 59% of the absorbed dose to the vertebrae and 62% for the hip bones, which means that purely blood-based dosimetry methods will underestimate the absorbed dose to the red marrow. Our blood-based estimates of 0.013 ± 0.006 Gy/GBq in patients without bone metastases are close to the median absorbed dose of 0.016 Gy/GBq reported for 200 patients in 2013, which was estimated by equating the activity concentrations in sequential blood samples to those of the bone marrow (190).

Surprisingly for patients with bone metastases, the estimated absorbed dose to the red marrow was higher and was estimated to be 0.085 ± 0.046 and 0.069 ± 0.033 Gy/GBq for the vertebrae and hip bones, respectively. The increase can plausibly be attributed to an increased presence of SSTR2 in the bone marrow from undetected micrometastases. Although larger tumors can be detected and avoided during the delineation process, the limited resolution of both SPECT and CT images makes it challenging to locate small tumors. Estimated at 0.017 ± 0.008 Gy/GBq, image-based methods did not demonstrate a comparable elevation in the absorbed dose to the red marrow for these patients.

In SPECT reconstructions, low-uptake areas will be especially noisy, which can be particularly harmful to the accuracy of the quantification in regions with low activity concentrations like the bone marrow. To minimize the effects of the noise, a decreasing number of iterations were used, from 20 to 6 (10 subsets), and evaluated for each skeletal site. Image-based red marrow dosimetry using SPECT usually utilizes the vertebrae for delineation because they are consistently present within the field of view. To obtain a more accurate estimate of the activity concentration, data can be collected from various skeletal sites (Fig. ). Beside the nine vertebrae, the hip bones were added as they are the largest reserve for red marrow and the cortical bone cavity is large enough to enable delineation. While we attempted and failed to consistently delineate the sternum as a third red marrow source, another study has utilized the proximal humerus in a hybrid imaging approach (186). The location of the proximal humerus avoids much of the physiological uptake in the abdomen and may therefore be suitable for planar image acquisitions.

The compartment model was also applied to one delineated tumor in each patient without bone metastases and a similar retention as the red marrow was observed (Fig. 24). The effective half-lives for the elimination phases of the vertebrae, hip bones, and tumor were estimated to be 94, 85, and 83 hours using an exponential fit. As other uptake mechanisms could contribute to the prolonged retention in the red marrow, transferrin being one them, another comparison was made between the effective half-lives of tumors compared to those for the vertebrae and hip bones. Since the transferrin mechanism acts to continuously transport iron or other metal ions like lutetium to the red marrow, a longer retention will follow. By subtracting the T1/2 for the tumor from that of the red marrow sites, patients with tumors exhibiting a fast elimination phase were found to have a statistically significant slower elimination phase for the red marrow activity compared to patients with tumors exhibiting a slow elimination phase.

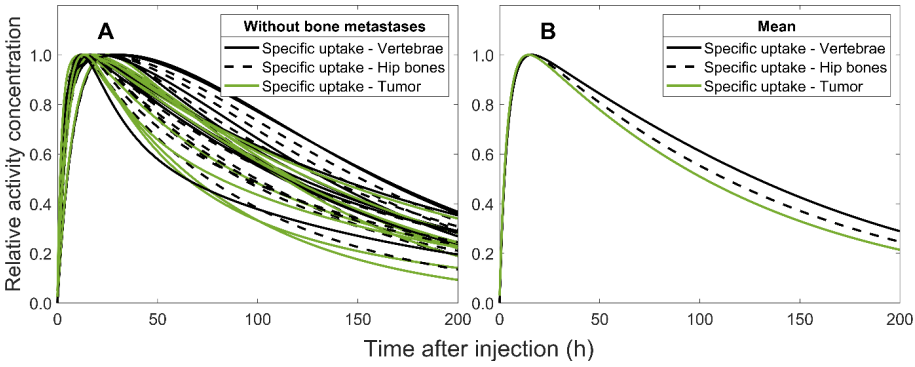


***FIGURE 24**. Results from the compartment model show the specific uptake in the vertebrae (solid), hip bones (dashed), and tumors (green) for each of the ten patients (A) without bone metastases and the respective mean (B).*

## SSTR2 – Antagonists

Our results of a considerable, and potentially SSTR2-related, uptake in [$^{177}$Lu]Lu-DOTATATE treatments are also interesting from the perspective of future SSTR2-based targeting agents. In a 2019 Phase 1 study, 20 patients diagnosed with NETs were treated with the SSTR2 antagonist [$^{177}$Lu]Lu-satoreotide tetraxetan (191). After the second treatment cycle, 4 out of the first 7 treated patients (57%) developed grade 4 thrombocytopenia. Although a small number of patients, this incidence is much higher compared to other studies and was not expected considering the administered activities were comparable to the 7.4 GBq/cycle (50-100 µg peptide mass) used in [$^{177}$Lu]Lu-DOTATATE treatments. The study utilized a blood-based approach, attempting to predict the red marrow absorbed dose using a pre-therapeutic injection of 1.85 GBq [$^{177}$Lu]Lu-satoreotide tetraxetan, assuming equivalent activity concentrations in blood samples and bone marrow. An interim analysis of another study involving [$^{177}$Lu]Lu-satoreotide tetraxetan (or DOTA-JR11) showed grade ¾ hematological toxicities in 34% of patients. The 35 patients included had less administered activity (4.5–6 GBq) and a varying peptide mass (300–1300 µg) (192). Increased tumor uptake has been observed preclinically when comparing SSTR2 antagonists to agonists such as octreotate (193). It is tempting to speculate that the increased uptake might not be limited to tumors but could perhaps extend to hematopoietic progenitor cells and explain the grade ¾ hematological toxicities. In contrast, results from a trial with 51 patients focusing on NETs using [$^{177}$Lu]Lu-DOTA-LM3, also an antagonist, demonstrate no signs of increased incidence of hematological toxicities compared to [$^{177}$Lu]Lu-DOTATATE-based regimens (194). Administered activities in that study ranged between 2.8 and 7.4 GBq (mean 6.1), with a mean peptide mass of 218 µg.

## Study IV

For terbium-161, the bone marrow model estimated the mean energy absorbed from cell-bound activity in CD34+ cells to be 2.04 keV/decay to the nucleus when distributed on the cell surface and 2.45 keV/decay when distributed in the cytoplasm, taking into account both self-dose and cross-irradiation from other cells. In cells without a nucleus, as in the original model, 16.1 keV/decay was delivered to the whole cell. When lutetium-177 was used instead, the mean absorbed energy in the nucleus from activity on the cell surface or in the cytoplasm was between 1.16 and 1.26 keV/decay and 3.86 keV/decay to the whole cell in cells without a nucleus. Although the spherical structures and centrally placed nuclei used in this model may not be particularly authentic, these results hint at the importance of modeling realistic cellular arrangements and activity distributions. For example, as the main contributor to the nucleus self-dose, a 2015 study demonstrated that the influence of Auger electrons can be diminished or enhanced depending on the positioning of the cell nuclei, although particularly for cell nuclei smaller than for hematopoietic stem cells (195). Accurate 3D modeling on small scales has been previously demonstrated, from individual cells to small tumors, but was not computationally realistic for the sizeable dimensions of the model in Study IV (196, 197).

As the distribution of $CD34^+$ cells is heterogeneous, the energy distribution resulting from specific uptake displays similar characteristics, successively decreasing as the concentration of $CD34^+$ cells decreases. Although still higher for all distances between 0-700 µm, the energy deposition gradient is steeper for terbium-161 as the influence of low-energy electrons lessens when the distance between cells increases. The spatial $CD34^+$ cell concentrations have been previously used in a skeletal dosimetry model but have not been applied to the modeling of individual cells (122). Only minor variations in the self-irradiation S values were demonstrated between evenly and heterogeneously distributed red marrow for three radionuclides in that study. However, discrepancies that become obvious when taking individual cells into account are toned down by the depth-weighted S values and 50 µm resolution (Fig. 25). While we used the distribution reported for the L1 vertebrae, the results are probably relevant for other skeletal sites as the patterns for the ribs and iliac crest in the original study were comparable (167).

For activity homogenously distributed throughout the extracellular space, i.e., non-specific uptake, the energy deposited to the $CD34^+$ nucleus was 10.94 kev/decay for terbium-161 and 8.62 keV/decay for lutetium-177, with a difference mainly due to the higher mean energy of the beta decay for terbium-161. This increase compared to the self-dose from specific uptake is a consequence of the relatively low packing density

of 0.55 achieved in the sphere packing. However, this is accounted for in the absorbed dose estimation through the rapid elimination of activity from the blood and the scaling using both the plasma volume fraction and packing density (Eq. 25).

The results from the bone marrow model were tested against the absorbed dose estimates from a patient in Study III where the methodology of specific and nonspecific uptake had been elaborated. The absorbed dose to red marrow from [$^{177}$Lu]Lu-DOTATATE, using S values from Study II, had been estimated to be 0.31 and 0.12 Gy for specific and nonspecific uptake and time-integrated activity concentrations of $3.44 \cdot 10^7$ and $1.36 \cdot 10^7$ decays/mL, respectively. For lutetium-177, the bone marrow model yielded estimates of absorbed doses of 0.20 Gy and 0.18 Gy from specific cytoplasmic and cell surface-bound uptake, respectively, and 0.04 Gy from nonspecific uptake. The equivalent bone marrow model absorbed dose for terbium-161 was 0.39 and 0.32 Gy from cytoplasmic and surface-bound uptake, respectively, and 0.05 Gy for nonspecific uptake. Based on the absorbed dose estimates using the bone marrow model, we found that lutetium-177 irradiation resulted in significantly lower absorbed dose (-50%), while terbium-161 yielded a similar absorbed dose compared to the previous study. However, to further analyze these results, a validation of the method in Study III using clinical response data from blood samples is necessary. The scaling procedure used in Eq. 24 has the advantage of being easily applicable to patient-specific parameters beyond activity concentrations, especially as the proposed bone marrow model expands to incorporate additional skeletal sites and bone marrow cellularities. As the concept of personalized dosimetry gains traction, it is critical for a dosimetry model to allow for individualization to stay relevant.

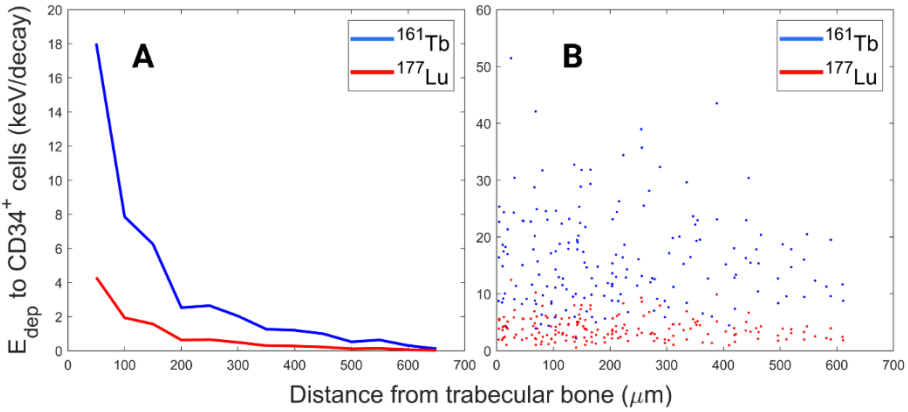


***FIGURE 25**. Energy deposition from the bone marrow model for terbium-161 (blue) and lutetium-177 (red) in 50μm voxels (A) and for each CD34⁺ cell in the radiation equilibrium region (B).*

# CONCLUSIONS

**Study I – Radioembolization**

Through the use of autoradiography and biopsy measurements, our study demonstrated that microsphere heterogeneity in a treated volume of HCC is significant and may not be accurately represented by mean absorbed dose estimates obtained from post-therapeutic bremsstrahlung SPECT/CT. Although the absorbed dose in poorly vascularized regions of the tumor was low, viable tumor tissue exhibited less variation in microsphere density, leading to mean absorbed doses exceeding the 120 Gy considered tumoricidal (72). The small region of normal tissue displayed a more homogeneous distribution with fewer microspheres. While not practical to perform routinely, biopsy measurements are valuable for understanding the limitations of radioembolization and identifying potential improvements.

**Study II, III, IV – Bone marrow dosimetry**

Study II revealed that the precision of determining activity distributions at a small scale significantly impacts the accuracy of subsequent absorbed dose estimates to the red bone marrow, particularly for radionuclides with a substantial contribution from low-energy electrons like terbium-161. Although yttrium-90 exhibited the highest S values overall, the increase in S values for terbium-161 relative to lutetium-171 was more dependent on the skeletal site. Furthermore, for patients with lower bone marrow cellularities than the reference values, which is probable for those undergoing PRRT, the S values for self-irradiation increased, potentially resulting in underestimations of the absorbed dose. A recent preclinical study involving DOTATATE and AR42J cells expressing SSTR has somewhat reinforced the conclusions of this study, as it demonstrated that the biodistribution was unaffected by the selection of either terbium-161 or lutetium-177 (15).

Using sequential SPECT imaging, we identified a prolonged retention of lutetium-177 in the spongy bone cavities of the vertebrae and hip bones, similar to that observed in tumors rather than blood. The uptake was hypothesized to be somatostatin receptor-related and therefore specific to the red marrow. However, an additional analysis demonstrated that the role of transferrin cannot be excluded when explaining bone marrow uptake. A compartment model was applied to separate the specific and non-specific uptake, demonstrating that a purely blood-based dosimetry approach will underestimate the absorbed dose to the red marrow.

By utilizing the results from Study III, we demonstrated the feasibility of a cell-based dosimetry model for the bone marrow. By simulating receptor-based specific uptake

in $CD34^+$ stem and progenitor cells and nonspecific uptake in the extracellular matrix, we showed that a transition from lutetium-177-based PRRT to terbium-161 without altering the administered activity per cycle will lead to an increased absorbed red marrow dose.

# FUTURE PERSPECTIVES

Based on the findings from the bone marrow studies, a number of potential approaches appear to hold promise for the next phase of bone marrow dosimetry following PRRT.

A reasonable first step, as the data already exists, is to statistically analyze the estimated absorbed dose to the red marrow in relation to the response data from blood sampling. Also, the dose estimates should be reinterpreted using the biologically effective dose concept. However, if the bone marrow dosimetry is to be truly individualized as well as reasonably efficient and realistic, utilization of existing images to estimate yellow marrow fractions in the vertebrae and hip bones is needed rather than collecting additional images. It is not unusual for patients to undergo diagnostic imaging prior to therapy, but at the moment, these images are not added to the dosimetry workflow. From my perspective, the development of a post-processing protocol for diagnostic dual-energy CT images seems more feasible than utilizing existing MRI images.

Although probably difficult due to the short half-life of gallium-68, it seems reasonable to attempt to utilize the [$^{68}$Ga]Ga-DOTATATE PET/CT images to verify the presence of SSTR2 in the red marrow. The use of longer-lived positron emitters is expected to be advantageous for such investigations. Similarly, the transferrin uptake mechanism is too slow for gallium-68, and one would first need to identify a specific red marrow uptake and then attempt to quantify the uptake in relation to red marrow estimates. If such a correlation existed and was established, pre-therapeutic bone marrow dosimetry could be realized.

The bone marrow model is potentially valuable, particularly if the specific uptake is confirmed as SSTR2-related, but it needs refinement and validation. Moving forward, the objective is to automate the simulation process and generate a database of energy deposition for the most commonly used radionuclides and varying bone marrow cellularities. This would be beneficial for forthcoming clinical trials that involve terbium-161, where bone marrow irradiation is a major concern.

# ACKNOWLEDGEMENTS

Först och främst vill jag tacka projektets finansiärer Cancerfonden, Konung Gustaf V:s Jubileumsfond, Vetenskapsrådet och Staten för Avtalet om Läkarutbildning och Forskning (ALF). Utan dessa ekonomiska bidrag skulle inget av forskningen som presenteras i denna avhandling varit möjlig.

Även om nyfikenheten alltid funnits där var det Peter Bernhardt som introducerade forskarvärlden och för detta är jag oerhört tacksam. Under de ungefär åtta år som vi har samarbetat har ditt idéflöde aldrig sinat och ditt driv och uppfinningsrikedom är inspirerande och emellanåt häpnadsväckande. Även Johanna Svensson har stor del i den glädjen jag fått uppleva i jobbet. Förutom ett bra bollplank, cancerlexikon och löparkompis har du varit utmärkt som bromskloss när Peter vill klämma in ett par projekt till. Jag vill även tacka Viktor Johansson och Johan Mölne för det vetenskapliga och proffsiga förhållningssätt som ni alltid tillämpar i era analyser och granskningar.

Som alla i branschen vet går forskning oftast inte rakt fram. Då är det fint att ha en bra forskargrupp runt omkring som underlättar tillvaron och gör det roligare att gå till jobbet. Ett STORT tack till Tobias (som är anledningen att vi äntligen bor i skärgården), Emma, Rebecca, Frida, Katja, Jakob, Jonas och Jehangir.

Jag vill också tacka många i ”radiofysikhuset” och i doktorandgruppen för all hjälp och stöd och trevliga stunder genom åren. Jag hoppas på många AW:s med er i framtiden.

Avslutningsvis vill jag tacka mina fina vänner och familj. För alla resor, allt fårvallande på Snugge, alla nätter i sommarsovsäck när det är minusgrader, toppturerna, för diskussionerna kring blåvitts senaste förlust, de fina somrarna på Öland och adrenalintillskottet på varje hösttur. Henning och Nils för att de ger mig många högkvalitativa pauser och vill brottas trots att det bara är en timma kvar tills tidsfristen löper ut och jag är stressad. Och Linn för att hon lyckas ha ett leende på läpparna mitt i det värsta flytt och renoveringskaoset. Tack för att du är en klippa och min bästa vän!

# REFERENCES


1. Brar G, Greten TF, Graubard BI, McNeel TS, Petrick JL, McGlynn KA, et al. Hepatocellular Carcinoma Survival by Etiology: A SEER-Medicare Database Analysis. Hepatol Commun. 2020;4(10):1541-51.
2. Llovet JM, Kelley RK, Villanueva A, Singal AG, Pikarsky E, Roayaie S, et al. Hepatocellular carcinoma. Nat Rev Dis Primers. 2021;7(1):6.
3. Global Burden of Disease Liver Cancer C, Akinyemiju T, Abera S, Ahmed M, Alam N, Alemayohu MA, et al. The Burden of Primary Liver Cancer and Underlying Etiologies From 1990 to 2015 at the Global, Regional, and National Level: Results From the Global Burden of Disease Study 2015. JAMA Oncol. 2017;3(12):1683-91.
4. Siegel RL, Miller KD, Jemal A. Cancer statistics, 2018. CA Cancer J Clin. 2018;68(1):7-30.
5. Van de Wiele C, Maes A, Brugman E, D'Asseler Y, De Spiegeleer B, Mees G, et al. SIRT of liver metastases: physiological and pathophysiological considerations. Eur J Nucl Med Mol Imaging. 2012;39(10):1646-55.
6. Bryce K, Tsochatzis EA. Downstaging for hepatocellular cancer: harm or benefit? Transl Gastroenterol Hepatol. 2017;2:106.
7. Oronsky B, Ma PC, Morgensztern D, Carter CA. Nothing But NET: A Review of Neuroendocrine Tumors and Carcinomas. Neoplasia. 2017;19(12):991-1002.
8. Leoncini E, Carioli G, La Vecchia C, Boccia S, Rindi G. Risk factors for neuroendocrine neoplasms: a systematic review and meta-analysis. Ann Oncol. 2016;27(1):68-81.
9. Dasari A, Shen C, Halperin D, Zhao B, Zhou S, Xu Y, et al. Trends in the Incidence, Prevalence, and Survival Outcomes in Patients With Neuroendocrine Tumors in the United States. JAMA Oncol. 2017;3(10):1335-42.
10. Genus TSE, Bouvier C, Wong KF, Srirajaskanthan R, Rous BA, Talbot DC, et al. Impact of neuroendocrine morphology on cancer outcomes and stage at diagnosis: a UK nationwide cohort study 2013-2015. Br J Cancer. 2019;121(11):966-72.
11. Khan MS, Pritchard DM. Neuroendocrine tumours: what gastroenterologists need to know. Frontline Gastroente. 2022;13(1):50-6.
12. Riihimaki M, Hemminki A, Sundquist K, Sundquist J, Hemminki K. The epidemiology of metastases in neuroendocrine tumors. Int J Cancer. 2016;139(12):2679-86.
13. Roobol SJ, van den Bent I, van Cappellen WA, Abraham TE, Paul MW, Kanaar R, et al. Comparison of High- and Low-LET Radiation-Induced

DNA Double-Strand Break Processing in Living Cells. Int J Mol Sci. 2020;21(18).
14. Selwyn RG, Nickles RJ, Thomadsen BR, DeWerd LA, Micka JA. A new internal pair production branching ratio of 90Y: the development of a non-destructive assay for 90Y and 90Sr. Appl Radiat Isot. 2007;65(3):318-27.
15. Borgna F, Barritt P, Grundler PV, Talip Z, Cohrs S, Zeevaart JR, et al. Simultaneous visualization of 161Tb-and 177Lu-Labeled somatostatin analogues using dual-isotope SPECT imaging. Pharmaceutics. 2021;13:536.
16. Eckerman K, Endo A. ICRP Publication 107. Nuclear decay data for dosimetric calculations. Ann ICRP. 2008;38(3):7-96.
17. Salvat F, Fernández-Varea JM, Sempau J, editors. PENELOPE-2006: A code system for Monte Carlo simulation of electron and photon transport. Workshop proceedings; 2006: Citeseer.
18. García-Toraño E, Peyres V, Salvat F. PenNuc: Monte Carlo simulation of the decay of radionuclides. Comput Phys Commun. 2019;245:106849.
19. Giménez-Alventosa V, Gómez VG, Oliver S. PenRed: An extensible and parallel Monte-Carlo framework for radiation transport based on PENELOPE. Computer Physics Communications. 2021;267:108065.
20. Salvat F. A generic algorithm for Monte Carlo simulation of proton transport. Nuclear Instruments & Methods in Physics Research Section B-beam Interactions With Materials and Atoms. 2013;316:144-59.
21. Asai M, Cortes-Giraldo MA, Gimenez-Alventosa V, Gomez VG, Salvat F. The PENELOPE Physics Models and Transport Mechanics. Implementation into Geant4. Front Phys-Lausanne. 2021;9.
22. Dickson JC, Armstrong IS, Gabina PM, Denis-Bacelar AM, Krizsan AK, Gear JM, et al. EANM practice guideline for quantitative SPECT-CT. European Journal of Nuclear Medicine and Molecular Imaging. 2023;50(4):980-95.
23. Kennedy JA, Lugassi R, Gill R, Keidar Z. Digital Solid-State SPECT/CT Quantitation of Absolute (177)Lu Radiotracer Concentration: In Vivo and In Vitro Validation. J Nucl Med. 2020;61(9):1381-7.
24. Koppert WJC, Dietze MMA, van der Velden S, Steenbergen JHL, de Jong H. A comparative study of NaI(Tl), CeBr(3), and CZT for use in a real-time simultaneous nuclear and fluoroscopic dual-layer detector. Phys Med Biol. 2019;64(13):135012.
25. Desmonts C, Bouthiba MA, Enilorac B, Nganoa C, Agostini D, Aide N. Evaluation of a new multipurpose whole-body CzT-based camera:

comparison with a dual-head Anger camera and first clinical images. EJNMMI Phys. 2020;7(1):18.
26. Kennedy J, Chicheportiche A, Keidar Z. Quantitative SPECT/CT for Dosimetry of Peptide Receptor Radionuclide Therapy. Semin Nucl Med. 2022;52(2):229-42.
27. Zeng GL. Maximum-Likelihood Expectation-Maximization Algorithm Versus Windowed Filtered Backprojection Algorithm: A Case Study. J Nucl Med Technol. 2018;46(2):129-32.
28. Hutton BF, Buvat I, Beekman FJ. Review and current status of SPECT scatter correction. Phys Med Biol. 2011;56(14):R85-112.
29. Gustafsson J, Brolin G, Ljungberg M. Monte Carlo-based SPECT reconstruction within the SIMIND framework. Physics in Medicine and Biology. 2018;63(24).
30. Rydén T, Heydorn Lagerlöf J, Hemmingsson J, Marin I, Svensson J, Båth M, et al. Fast GPU-based Monte Carlo code for SPECT/CT reconstructions generates improved 177Lu images. EJNMMI Phys. 2018;5:1-12.
31. Grings A, Jobic C, Kuwert T, Ritt P. The magnitude of the partial volume effect in SPECT imaging of the kidneys: a phantom study. EJNMMI Phys. 2022;9(1):18.
32. Ljungberg M, Gleisner KS. 3-D Image-Based Dosimetry in Radionuclide Therapy. Ieee T Radiat Plasma. 2018;2(6):527-40.
33. Hindorf C, Glatting G, Chiesa C, Lindén O, Flux G. EANM Dosimetry Committee guidelines for bone marrow and whole-body dosimetry. Eur J Nucl Med Mol Imaging. 2010;37:1238-50.
34. Loevinger R, Budinger TF, Watson EE, Society of Nuclear Medicine . Medical Internal Radiation Dose C. MIRD primer for absorbed dose calculations. Rev. ed ed. New York, NY: Society of Nuclear Medicine; 1991. xiii, 128 p. : ill. p.
35. Bolch WE, Eckerman KF, Sgouros G, Thomas SR. MIRD pamphlet No. 21: a generalized schema for radiopharmaceutical dosimetry--standardization of nomenclature. J Nucl Med. 2009;50(3):477-84.
36. Sjogreen Gleisner K, Chouin N, Gabina PM, Cicone F, Gnesin S, Stokke C, et al. EANM dosimetry committee recommendations for dosimetry of 177Lu-labelled somatostatin-receptor- and PSMA-targeting ligands. Eur J Nucl Med Mol Imaging. 2022;49(6):1778-809.
37. Konijnenberg M, Herrmann K, Kobe C, Verburg F, Hindorf C, Hustinx R, et al. EANM position paper on article 56 of the Council Directive 2013/59/Euratom (basic safety standards) for nuclear medicine therapy. Eur J Nucl Med Mol Imaging. 2021;48(1):67-72.

38. Anjos-Afonso F, Bonnet D. Human CD34+ hematopoietic stem cell hierarchy: how far are we with its delineation at the most primitive level? Blood. 2023.
39. Higgins JM. Red blood cell population dynamics. Clin Lab Med. 2015;35(1):43-57.
40. Griffith JF. Bone marrow changes in osteoporosis. Osteoporosis and Bone Densitometry Measurements: Springer; 2013. p. 69-85.
41. Carmona R, Pritz J, Bydder M, Gulaya S, Zhu H, Williamson CW, et al. Fat composition changes in bone marrow during chemotherapy and radiation therapy. Int J Radiat Oncol Biol Phys. 2014;90(1):155-63.
42. Valentine WN, Pearce ML, Lawrence JS. Studies on the radiosensitivity of bone marrow. II. The effect of large, repeated whole body irradiation exposure on hematopoiesis. Blood. 1952;7(1):14-9.
43. Ishikawa J, Hayashi N, Yamaguchi M, Monzen S, Kashiwakura I. Characteristics of human CD34+ cells exposed to ionizing radiation under cytokine-free conditions. J Radiat Res. 2015;56(4):678-90.
44. Kato K, Omori A, Kashiwakura I. Radiosensitivity of human haematopoietic stem/progenitor cells. J Radiol Prot. 2013;33(1):71-80.
45. Lautt WW. Hepatic Circulation: Physiology and Pathophysiology. Colloquium Series on Integrated Systems Physiology: From Molecule to Function to Disease. San Rafael (CA)2009.
46. Kennedy A, Bester L, Salem R, Sharma RA, Parks RW, Ruszniewski P, et al. Role of hepatic intra-arterial therapies in metastatic neuroendocrine tumours (NET): guidelines from the NET-Liver-Metastases Consensus Conference. HPB (Oxford). 2015;17(1):29-37.
47. Lee EW, Alanis L, Cho SK, Saab S. Yttrium-90 Selective Internal Radiation Therapy with Glass Microspheres for Hepatocellular Carcinoma: Current and Updated Literature Review. Korean J Radiol. 2016;17(4):472-88.
48. Debbaut C, Segers P, Cornillie P, Casteleyn C, Dierick M, Laleman W, et al. Analyzing the human liver vascular architecture by combining vascular corrosion casting and micro-CT scanning: a feasibility study. J Anat. 2014;224(4):509-17.
49. Hogberg J, Rizell M, Hultborn R, Svensson J, Henrikson O, Molne J, et al. Increased absorbed liver dose in Selective Internal Radiation Therapy (SIRT) correlates with increased sphere-cluster frequency and absorbed dose inhomogeneity. EJNMMI Phys. 2015;2(1):10.
50. Reinders MTM, Smits MLJ, van Roekel C, Braat A. Holmium-166 Microsphere Radioembolization of Hepatic Malignancies. Semin Nucl Med. 2019;49(3):237-43.

51. Wasan HS, Gibbs P, Sharma NK, Taieb J, Heinemann V, Ricke J, et al. First-line selective internal radiotherapy plus chemotherapy versus chemotherapy alone in patients with liver metastases from colorectal cancer (FOXFIRE, SIRFLOX, and FOXFIRE-Global): a combined analysis of three multicentre, randomised, phase 3 trials. Lancet Oncol. 2017;18(9):1159-71.
52. Fabritius MP, Ricke J. Overview of Ongoing Clinical Trials on Radioembolization. Cardiovasc Intervent Radiol. 2022;45(11):1659-62.
53. Gray B, Van Hazel G, Hope M, Burton M, Moroz P, Anderson J, et al. Randomised trial of SIR-Spheres plus chemotherapy vs. chemotherapy alone for treating patients with liver metastases from primary large bowel cancer. Ann Oncol. 2001;12(12):1711-20.
54. Hendlisz A, Van den Eynde M, Peeters M, Maleux G, Lambert B, Vannoote J, et al. Phase III Trial Comparing Protracted Intravenous Fluorouracil Infusion Alone or With Yttrium-90 Resin Microspheres Radioembolization for Liver-Limited Metastatic Colorectal Cancer Refractory to Standard Chemotherapy. Journal of Clinical Oncology. 2010;28(23):3687-94.
55. Dhondt E, Lambert B, Hermie L, Huyck L, Vanlangenhove P, Geerts A, et al. (90)Y Radioembolization versus Drug-eluting Bead Chemoembolization for Unresectable Hepatocellular Carcinoma: Results from the TRACE Phase II Randomized Controlled Trial. Radiology. 2022;303(3):699-710.
56. Salem R, Lewandowski RJ, Kulik L, Wang E, Riaz A, Ryu RK, et al. Radioembolization results in longer time-to-progression and reduced toxicity compared with chemoembolization in patients with hepatocellular carcinoma. Gastroenterology. 2011;140(2):497-507 e2.
57. Edeline J, Touchefeu Y, Guiu B, Farge O, Tougeron D, Baumgaertner I, et al. Radioembolization Plus Chemotherapy for First-line Treatment of Locally Advanced Intrahepatic Cholangiocarcinoma: A Phase 2 Clinical Trial. JAMA Oncol. 2020;6(1):51-9.
58. Ettorre GM, Levi Sandri GB, Laurenzi A, Colasanti M, Meniconi RL, Lionetti R, et al. Yttrium-90 Radioembolization for Hepatocellular Carcinoma Prior to Liver Transplantation. World J Surg. 2017;41(1):241-9.
59. Cucchetti A, Elshaarawy O, Han G, Chong CCN, Serra C, O'Rourke JM, et al. 'Potentially curative therapies' for hepatocellular carcinoma: how many patients can actually be cured? Br J Cancer. 2023.
60. Garin E, Rolland Y, Laffont S, Edeline J. Clinical impact of (99m)Tc-MAA SPECT/CT-based dosimetry in the radioembolization of liver

malignancies with (90)Y-loaded microspheres. Eur J Nucl Med Mol Imaging. 2016;43(3):559-75.
61. Gill H, Hiller J. Systematic review of lung shunt fraction quantification comparing SPECT/CT and planar scintigraphy for yttrium 90 radioembolization planning. Clin Transl Imaging. 2021;9(2):181-8.
62. Chiesa C, Sjogreen-Gleisner K, Walrand S, Strigari L, Flux G, Gear J, et al. EANM dosimetry committee series on standard operational procedures: a unified methodology for (99m)Tc-MAA pre- and (90)Y peri-therapy dosimetry in liver radioembolization with (90)Y microspheres. EJNMMI Phys. 2021;8(1):77.
63. Cremonesi M, Chiesa C, Strigari L, Ferrari M, Botta F, Guerriero F, et al. Radioembolization of hepatic lesions from a radiobiology and dosimetric perspective. Front Oncol. 2014;4:210.
64. Bastiaannet R, Kappadath SC, Kunnen B, Braat A, Lam M, de Jong H. The physics of radioembolization. EJNMMI Phys. 2018;5(1):22.
65. Siman W, Mikell JK, Kappadath SC. Practical reconstruction protocol for quantitative (90)Y bremsstrahlung SPECT/CT. Med Phys. 2016;43(9):5093.
66. Ince C, Karadeniz O, Ertay T, Durak H. Collimator and energy window optimization for YTTRIUM-90 bremsstrahlung SPECT imaging. Appl Radiat Isot. 2021;167:109453.
67. Porter CA, Bradley KM, Hippelainen ET, Walker MD, McGowan DR. Phantom and clinical evaluation of the effect of full Monte Carlo collimator modelling in post-SIRT yttrium-90 Bremsstrahlung SPECT imaging. EJNMMI Res. 2018;8(1):7.
68. Kao YH, Steinberg JD, Tay YS, Lim GK, Yan J, Townsend DW, et al. Post-radioembolization yttrium-90 PET/CT- part 2: dose-response and tumor predictive dosimetry for resin microspheres. EJNMMI Res. 2013;3(1):57.
69. Wondergem M, Smits ML, Elschot M, de Jong HW, Verkooijen HM, van den Bosch MA, et al. 99mTc-macroaggregated albumin poorly predicts the intrahepatic distribution of 90Y resin microspheres in hepatic radioembolization. J Nucl Med. 2013;54(8):1294-301.
70. Ulrich G, Dudeck O, Furth C, Ruf J, Grosser OS, Adolf D, et al. Predictive value of intratumoral 99mTc-macroaggregated albumin uptake in patients with colorectal liver metastases scheduled for radioembolization with 90Y-microspheres. J Nucl Med. 2013;54(4):516-22.
71. Chiesa C, Mira M, Maccauro M, Spreafico C, Romito R, Morosi C, et al. Radioembolization of hepatocarcinoma with (90)Y glass microspheres: development of an individualized treatment planning strategy based on dosimetry and radiobiology. Eur J Nucl Med Mol Imaging. 2015;42(11):1718-38.

72. Garin E, Guiu B, Edeline J, Rolland Y, Palard X. Trans-arterial Radioembolization Dosimetry in 2022. Cardiovasc Intervent Radiol. 2022;45(11):1608-21.
73. Sangro B, Gil-Alzugaray B, Rodriguez J, Sola I, Martinez-Cuesta A, Viudez A, et al. Liver disease induced by radioembolization of liver tumors: description and possible risk factors. Cancer. 2008;112(7):1538-46.
74. Levillain H, Bagni O, Deroose CM, Dieudonne A, Gnesin S, Grosser OS, et al. International recommendations for personalised selective internal radiation therapy of primary and metastatic liver diseases with yttrium-90 resin microspheres. Eur J Nucl Med Mol Imaging. 2021;48(5):1570-84.
75. Walrand S, Hesse M, d'Abadie P, Jamar F. Hepatic Arterial Buffer Response in Liver Radioembolization and Potential Use for Improved Cancer Therapy. Cancers (Basel). 2021;13(7).
76. Braat MN, van Erpecum KJ, Zonnenberg BA, van den Bosch MA, Lam MG. Radioembolization-induced liver disease: a systematic review. Eur J Gastroenterol Hepatol. 2017;29(2):144-52.
77. Pan MM, Gabr A, Riaz A, Mouli S, Salem R, Lewandowski RJ. Does significantly elevated lung shunt fraction (LSF> 20%) promote extrahepatic progression in patients with hepatocellular carcinoma treated with radioembolization? Nuclear Medicine Communications. 2021;42(7):725-31.
78. Reubi JC, Waser B. Concomitant expression of several peptide receptors in neuroendocrine tumours: molecular basis for in vivo multireceptor tumour targeting. European journal of nuclear medicine and molecular imaging. 2003;30:781-93.
79. Reubi JC. Peptide receptor expression in GEP-NET. Virchows Arch. 2007;451 Suppl 1:S47-50.
80. Oomen S, Hofland L, van Hagen M, Lamberts S, Touw I. Somatostatin receptors in the haematopoietic system. Eur J Endocrinol. 2000;143:9-14.
81. Oomen SP, van Hennik PB, Antonissen C, Lichtenauer-Kaligis EG, Hofland LJ, Lamberts SW, et al. Somatostatin is a selective chemoattractant for primitive (CD34+) hematopoietic progenitor cells. Exp Hematol. 2002;30:116-25.
82. Gunther T, Tulipano G, Dournaud P, Bousquet C, Csaba Z, Kreienkamp HJ, et al. International Union of Basic and Clinical Pharmacology. CV. Somatostatin Receptors: Structure, Function, Ligands, and New Nomenclature. Pharmacol Rev. 2018;70(4):763-835.
83. Patel YC. Somatostatin and its receptor family. Front Neuroendocrinol. 1999;20(3):157-98.

84. Esser J-P, Krenning E, Teunissen J, Kooij P, Van Gameren A, Bakker W, et al. Comparison of [177 Lu-DOTA 0, Tyr 3] octreotate and [177 Lu-DOTA 0, Tyr 3] octreotide: which peptide is preferable for PRRT? European journal of nuclear medicine and molecular imaging. 2006;33:1346-51.
85. Capello A, Krenning EP, Breeman WA, Bernard BF, Konijnenberg MW, de Jong M. Tyr3-octreotide and Tyr3-octreotate radiolabeled with 177Lu or 90Y: peptide receptor radionuclide therapy results in vitro. Cancer Biother Radiopharm. 2003;18(5):761-8.
86. Cwikla JB, Sankowski A, Seklecka N, Buscombe JR, Nasierowska-Guttmejer A, Jeziorski KG, et al. Efficacy of radionuclide treatment DOTATATE Y-90 in patients with progressive metastatic gastroenteropancreatic neuroendocrine carcinomas (GEP-NETs): a phase II study. Ann Oncol. 2010;21(4):787-94.
87. Imhof A, Brunner P, Marincek N, Briel M, Schindler C, Rasch H, et al. Response, survival, and long-term toxicity after therapy with the radiolabeled somatostatin analogue [90Y-DOTA]-TOC in metastasized neuroendocrine cancers. J Clin Oncol. 2011;29(17):2416-23.
88. Kwekkeboom DJ, de Herder WW, Kam BL, van Eijck CH, van Essen M, Kooij PP, et al. Treatment with the radiolabeled somatostatin analog [177Lu-DOTA0, Tyr3] octreotate: toxicity, efficacy, and survival. Journal of Clinical Oncology. 2008;26(13):2124-30.
89. Pfeifer AK, Gregersen T, Grønbæk H, Hansen CP, Müller-Brand J, Bruun KH, et al. Peptide receptor radionuclide therapy with 90Y-DOTATOC and 177Lu-DOTATOC in advanced neuroendocrine tumors: results from a Danish cohort treated in Switzerland. Neuroendocrinology. 2011;93(3):189-96.
90. Ezziddin S, Attassi M, Yong-Hing CJ, Ahmadzadehfar H, Willinek W, Grunwald F, et al. Predictors of long-term outcome in patients with well-differentiated gastroenteropancreatic neuroendocrine tumors after peptide receptor radionuclide therapy with 177Lu-octreotate. J Nucl Med. 2014;55(2):183-90.
91. Strosberg J, El-Haddad G, Wolin E, Hendifar A, Yao J, Chasen B, et al. Phase 3 trial of 177Lu-Dotatate for midgut neuroendocrine tumors. New England Journal of Medicine. 2017;376(2):125-35.
92. Bodei L, Ambrosini V, Herrmann K, Modlin I. Current concepts in 68Ga-DOTATATE imaging of neuroendocrine neoplasms: interpretation, biodistribution, dosimetry, and molecular strategies. Journal of Nuclear Medicine. 2017;58(11):1718-26.
93. Kratochwil C, Stefanova M, Mavriopoulou E, Holland-Letz T, Dimitrakopoulou-Strauss A, Afshar-Oromieh A, et al. SUV of [68 Ga] DOTATOC-PET/CT predicts response probability of PRRT in

neuroendocrine tumors. Molecular Imaging and Biology. 2015;17:313-8.

94. Srirajaskanthan R, Kayani I, Quigley AM, Soh J, Caplin ME, Bomanji J. The role of 68Ga-DOTATATE PET in patients with neuroendocrine tumors and negative or equivocal findings on 111In-DTPA-octreotide scintigraphy. Journal of Nuclear Medicine. 2010;51(6):875-82.

95. Haug AR, Cindea-Drimus R, Auernhammer CJ, Reincke M, Wängler B, Uebleis C, et al. The role of 68Ga-DOTATATE PET/CT in suspected neuroendocrine tumors. Journal of nuclear medicine. 2012;53(11):1686-92.

96. Haug AR, Cindea-Drimus R, Auernhammer CJ, Reincke M, Beuschlein F, Wängler B, et al. Neuroendocrine tumor recurrence: diagnosis with 68Ga-DOTATATE PET/CT. Radiology. 2014;270(2):517-25.

97. Lee ONY, Tan KV, Tripathi V, Yuan H, Chan WW-L, Chiu KWH. The Role of 68Ga-DOTA-SSA PET/CT in the management and prediction of peptide receptor radionuclide therapy response for patients with neuroendocrine tumors: a systematic review and meta-analysis. Clinical Nuclear Medicine. 2022;47(9):781-93.

98. Stenvall A, Gustafsson J, Larsson E, Roth D, Sundlöv A, Jönsson L, et al. Relationships between uptake of [68Ga] Ga-DOTA-TATE and absorbed dose in [177Lu] Lu-DOTA-TATE therapy. EJNMMI research. 2022;12(1):1-15.

99. Chan DL, Pavlakis N, Schembri GP, Bernard EJ, Hsiao E, Hayes A, et al. Dual Somatostatin Receptor/FDG PET/CT Imaging in Metastatic Neuroendocrine Tumours: Proposal for a Novel Grading Scheme with Prognostic Significance. Theranostics. 2017;7(5):1149-58.

100. Bodei L, Raj N, Do RK, Mauguen A, Krebs S, Reidy-Lagunes D, et al. Interim Analysis of a Prospective Validation of 2 Blood-Based Genomic Assessments (PPQ and NETest) to Determine the Clinical Efficacy of (177)Lu-DOTATATE in Neuroendocrine Tumors. J Nucl Med. 2023;64(4):567-73.

101. Morphis M, van Staden JA, du Raan H, Ljungberg M. Evaluation of Iodine-123 and Iodine-131 SPECT activity quantification: a Monte Carlo study. EJNMMI Phys. 2021;8(1):61.

102. Muller C, Vermeulen C, Koster U, Johnston K, Turler A, Schibli R, et al. Alpha-PET with terbium-149: evidence and perspectives for radiotheragnostics. EJNMMI Radiopharm Chem. 2017;1(1):5.

103. Baum RP, Singh A, Benesova M, Vermeulen C, Gnesin S, Koster U, et al. Clinical evaluation of the radiolanthanide terbium-152: first-in-human PET/CT with (152)Tb-DOTATOC. Dalton Trans. 2017;46(42):14638-46.

104. Favaretto C, Talip Z, Borgna F, Grundler PV, Dellepiane G, Sommerhalder A, et al. Cyclotron production and radiochemical

purification of terbium-155 for SPECT imaging. EJNMMI Radiopharm Chem. 2021;6(1):37.
105. Grosser OS, Ruf J, Pethe A, Kupitz D, Wissel H, Benckert C, et al. Urinary Excretion of Yttrium-90 after Radioembolization with Yttrium-90-Labeled Resin-based Microspheres. Health Phys. 2018;114(1):58-63.
106. Sandström M, Freedman N, Frösss-Baron K, Kahn T, Sundin A. Kidney dosimetry in 777 patients during 177 Lu-DOTATATE therapy: aspects on extrapolations and measurement time points. EJNMMI physics. 2020;7:1-15.
107. Benua RS, Cicale NR, Sonenberg M, Rawson RW. The relation of radioiodine dosimetry to results and complications in the treatment of metastatic thyroid cancer. Am J Roentgenol Radium Ther Nucl Med. 1962;87:171-82.
108. Lassmann M, Hanscheid H, Chiesa C, Hindorf C, Flux G, Luster M, et al. EANM Dosimetry Committee series on standard operational procedures for pre-therapeutic dosimetry I: blood and bone marrow dosimetry in differentiated thyroid cancer therapy. Eur J Nucl Med Mol Imaging. 2008;35(7):1405-12.
109. Sgouros G. Bone marrow dosimetry for radioimmunotherapy: theoretical considerations. J Nucl Med. 1993;34(4):689-94.
110. Forrer F, Krenning EP, Kooij PP, Bernard BF, Konijnenberg M, Bakker WH, et al. Bone marrow dosimetry in peptide receptor radionuclide therapy with [177Lu-DOTA(0),Tyr(3)]octreotate. Eur J Nucl Med Mol Imaging. 2009;36(7):1138-46.
111. Del Prete M, Arsenault F, Saighi N, Zhao W, Buteau FA, Celler A, et al. Accuracy and reproducibility of simplified QSPECT dosimetry for personalized (177)Lu-octreotate PRRT. EJNMMI Phys. 2018;5(1):25.
112. Chicheportiche A, Ben-Haim S, Grozinsky-Glasberg S, Oleinikov K, Meirovitz A, Gross DJ, et al. Dosimetry after peptide receptor radionuclide therapy: impact of reduced number of post-treatment studies on absorbed dose calculation and on patient management. EJNMMI Phys. 2020;7(1):5.
113. Svensson J, Ryden T, Hagmarker L, Hemmingsson J, Wangberg B, Bernhardt P. A novel planar image-based method for bone marrow dosimetry in (177)Lu-DOTATATE treatment correlates with haematological toxicity. EJNMMI Phys. 2016;3(1):21.
114. Hagmarker L, Svensson J, Rydén T, van Essen M, Sundlöv A, Gleisner KS, et al. Bone marrow absorbed doses and correlations with hematologic response during 177Lu-DOTATATE treatments are influenced by image-based dosimetry method and presence of skeletal metastases. J Nucl Med. 2019;60:1406-13.

115. Spiers F. BETA PARTICLE DOSIMETRY IN TRABECULAR BONE. Univ. of Leeds, Eng.; 1969.
116. Bouchet LG, Jokisch DW, Bolch WE. A three-dimensional transport model for determining absorbed fractions of energy for electrons within trabecular bone. Journal of Nuclear Medicine. 1999;40(11):1947-66.
117. Shah AP, Bolch WE, Rajon DA, Patton PW, Jokisch DW. A paired-image radiation transport model for skeletal dosimetry. Journal of Nuclear Medicine. 2005;46(2):344-53.
118. Pafundi D, Rajon D, Jokisch D, Lee C, Bolch W. An image-based skeletal dosimetry model for the ICRP reference newborn--internal electron sources. Phys Med Biol. 2010;55(7):1785-814.
119. Hough M, Johnson P, Rajon D, Jokisch D, Lee C, Bolch W. An image-based skeletal dosimetry model for the ICRP reference adult male--internal electron sources. Phys Med Biol. 2011;56(8):2309-46.
120. O'Reilly SE, DeWeese LS, Maynard MR, Rajon DA, Wayson MB, Marshall EL, et al. An image-based skeletal dosimetry model for the ICRP reference adult female-internal electron sources. Phys Med Biol. 2016;61(24):8794-824.
121. Geyer AM, Schwarz BC, Hobbs RF, Sgouros G, Bolch WE. Quantitative impact of changes in marrow cellularity, skeletal size, and bone mineral density on active marrow dosimetry based upon a reference model. Med Phys. 2017;44(1):272-83.
122. Geyer AM, Schwarz BC, O'Reilly SE, Hobbs RF, Sgouros G, Bolch WE. Depth-dependent concentrations of hematopoietic stem cells in the adult skeleton: Implications for active marrow dosimetry. Medical physics. 2017;44(2):747-61.
123. Page E. Impact of 3D Image Based Dosimetry on Treatment Planning in Peptide Receptor Radionuclide Therapy (PRRT): University of Manchester; 2020.
124. Gosewisch A, Ilhan H, Tattenberg S, Mairani A, Parodi K, Brosch J, et al. 3D Monte Carlo bone marrow dosimetry for Lu-177-PSMA therapy with guidance of non-invasive 3D localization of active bone marrow via Tc-99m-anti-granulocyte antibody SPECT/CT. EJNMMI Res. 2019;9:1-14.
125. Heylmann D, Ponath V, Kindler T, Kaina B. Comparison of DNA repair and radiosensitivity of different blood cell populations. Sci Rep. 2021;11(1):2478.
126. Garske-Román U, Sandström M, Fröss Baron K, Lundin L, Hellman P, Welin S, et al. Prospective observational study of 177Lu-DOTA-octreotate therapy in 200 patients with advanced metastasized neuroendocrine tumours (NETs): feasibility and impact of a

dosimetry-guided study protocol on outcome and toxicity. Eur J Nucl Med Mol Imaging. 2018;45:970-88.

127. Cremonesi M, Ferrari ME, Bodei L, Chiesa C, Sarnelli A, Garibaldi C, et al. Correlation of dose with toxicity and tumour response to (90)Y- and (177)Lu-PRRT provides the basis for optimization through individualized treatment planning. Eur J Nucl Med Mol Imaging. 2018;45(13):2426-41.

128. Del Prete M, Buteau F-A, Arsenault F, Saighi N, Bouchard L-O, Beaulieu A, et al. Personalized 177Lu-octreotate peptide receptor radionuclide therapy of neuroendocrine tumours: initial results from the P-PRRT trial. Eur J Nucl Med Mol Imaging. 2019;46:728-42.

129. Svensson J, Hagmarker L, Magnander T, Wängberg B, Bernhardt P. Radiation exposure of the spleen during 177Lu-DOTATATE treatment and its correlation with haematological toxicity and spleen volume. EJNMMI Phys. 2016;3:1-9.

130. Morland D, Triumbari EKA, Hoog C, Sezin G, Dejust S, Cadiot G, et al. Predicting subacute hematological toxicity of 177Lu-DOTATATE therapy using healthy organs' uptake on post-treatment quantitative SPECT: A pilot study. Medicine (Baltimore). 2022;101(49):e32212.

131. Bodei L, Kidd M, Paganelli G, Grana CM, Drozdov I, Cremonesi M, et al. Long-term tolerability of PRRT in 807 patients with neuroendocrine tumours: the value and limitations of clinical factors. Eur J Nucl Med Mol Imaging. 2015;42:5-19.

132. Strosberg JR, Caplin ME, Kunz PL, Ruszniewski PB, Bodei L, Hendifar A, et al. 177Lu-Dotatate plus long-acting octreotide versus high-dose long-acting octreotide in patients with midgut neuroendocrine tumours (NETTER-1): final overall survival and long-term safety results from an open-label, randomised, controlled, phase 3 trial. The Lancet Oncology. 2021;22(12):1752-63.

133. Bergsma H, Konijnenberg MW, Kam BL, Teunissen JJ, Kooij PP, de Herder WW, et al. Subacute haematotoxicity after PRRT with 177 Lu-DOTA-octreotate: prognostic factors, incidence and course. European journal of nuclear medicine and molecular imaging. 2016;43:453-63.

134. Svensson J, Berg G, Wängberg B, Larsson M, Forssell-Aronsson E, Bernhardt P. Renal function affects absorbed dose to the kidneys and haematological toxicity during 177 Lu-DOTATATE treatment. European journal of nuclear medicine and molecular imaging. 2015;42:947-55.

135. Sabet A, Ezziddin K, Pape U-F, Ahmadzadehfar H, Mayer K, Pöppel T, et al. Long-term hematotoxicity after peptide receptor radionuclide therapy with 177Lu-octreotate. J Nucl Med. 2013;54:1857-61.

136. Sgouros G, Bolch WE, Chiti A, Dewaraja YK, Emfietzoglou D, Hobbs RF, et al. ICRU REPORT 96, dosimetry-guided radiopharmaceutical therapy. Journal of the ICRU. 2021;21(1):1-212.
137. Tamborino G, De Saint-Hubert M, Struelens L, Seoane DC, Ruigrok EA, Aerts A, et al. Cellular dosimetry of [177 Lu] Lu-DOTA-[Tyr 3] octreotate radionuclide therapy: the impact of modeling assumptions on the correlation with in vitro cytotoxicity. EJNMMI physics. 2020;7:1-19.
138. Hayman JA, Callahan JW, Herschtal A, Everitt S, Binns DS, Hicks RJ, et al. Distribution of proliferating bone marrow in adult cancer patients determined using FLT-PET imaging. Int J Radiat Oncol Biol Phys. 2011;79(3):847-52.
139. Campbell BA, Callahan J, Bressel M, Simoens N, Everitt S, Hofman MS, et al. Distribution Atlas of Proliferating Bone Marrow in Non-Small Cell Lung Cancer Patients Measured by FLT-PET/CT Imaging, With Potential Applicability in Radiation Therapy Planning. Int J Radiat Oncol Biol Phys. 2015;92(5):1035-43.
140. Van Loon K, Zhang L, Keiser J, Carrasco C, Glass K, Ramirez M-T, et al. Bone metastases and skeletal-related events from neuroendocrine tumors. Endocrine Connections. 2015;4(1):9.
141. Lebtahi R, Cadiot G, Delahaye N, Genin R, Daou D, Peker MC, et al. Detection of bone metastases in patients with endocrine gastroenteropancreatic tumors: bone scintigraphy compared with somatostatin receptor scintigraphy. J Nucl Med. 1999;40(10):1602-8.
142. Rizzo FM, Vesely C, Childs A, Marafioti T, Khan MS, Mandair D, et al. Circulating tumour cells and their association with bone metastases in patients with neuroendocrine tumours. British journal of cancer. 2019;120(3):294-300.
143. Das S, Du L, Schad A, Jain S, Jessop A, Shah C, et al. A clinical score for neuroendocrine tumor patients under consideration for Lu-177-DOTATATE therapy. Endocr Relat Cancer. 2021;28(3):203-12.
144. Baum T, Yap SP, Dieckmeyer M, Ruschke S, Eggers H, Kooijman H, et al. Assessment of whole spine vertebral bone marrow fat using chemical shift-encoding based water-fat MRI. Journal of Magnetic Resonance Imaging. 2015;42(4):1018-23.
145. Salas-Ramirez M, Tran-Gia J, Kesenheimer C, Weng AM, Kosmala A, Heidemeier A, et al. Quantification of fat fraction in lumbar vertebrae: correlation with age and implications for bone marrow dosimetry in molecular radiotherapy. Phys Med Biol. 2018;63:025029.
146. Liu Z, Huang D, Zhang Y, Chang R, Zhang X, Jiang Y, et al. Accuracy and applicability of dual-energy computed tomography in

quantifying vertebral bone marrow adipose tissue compared with magnetic resonance imaging. Insights into Imaging. 2022;13:181.
147. Griffith JF, Yeung DK, Ma HT, Leung JC, Kwok TC, Leung PC. Bone marrow fat content in the elderly: a reversal of sex difference seen in younger subjects. J Magn Reson Imaging. 2012;36(1):225-30.
148. Kugel H, Jung C, Schulte O, Heindel W. Age-and sex-specific differences in the 1H-spectrum of vertebral bone marrow. JMRI. 2001;13:263-8.
149. Baum T, Yap SP, Dieckmeyer M, Ruschke S, Eggers H, Kooijman H, et al. Assessment of whole spine vertebral bone marrow fat using chemical shift-encoding based water-fat MRI. JMRI. 2015;42(4):1018-23.
150. Ognard J, Demany N, Mesrar J, Aho-Glele LS, Saraux A, Ben Salem D. Mapping the medullar adiposity of lumbar spine in MRI: A feasibility study. Heliyon. 2021;7(1):e05992.
151. Li X, Kuo D, Schafer AL, Porzig A, Link TM, Black D, et al. Quantification of vertebral bone marrow fat content using 3 Tesla MR spectroscopy: reproducibility, vertebral variation, and applications in osteoporosis. J Magn Reson Imaging. 2011;33(4):974-9.
152. Bain BJ. Bone marrow aspiration. J Clin Pathol. 2001;54(9):657-63.
153. Hwang S, Panicek DM. Magnetic resonance imaging of bone marrow in oncology, Part 1. Skeletal Radiol. 2007;36(10):913-20.
154. Karampinos DC, Ruschke S, Dieckmeyer M, Diefenbach M, Franz D, Gersing AS, et al. Quantitative MRI and spectroscopy of bone marrow. J Magn Reson Imaging. 2018;47(2):332-53.
155. Torkian P, Azadbakht J, Andrea Bonaffini P, Amini B, Chalian M. Advanced Imaging in Multiple Myeloma: New Frontiers for MRI. Diagnostics (Basel). 2022;12(9).
156. Reeder SB, Hu HH, Sirlin CB. Proton density fat-fraction: a standardized MR-based biomarker of tissue fat concentration. J Magn Reson Imaging. 2012;36(5):1011-4.
157. Hernando D, Sharma SD, Aliyari Ghasabeh M, Alvis BD, Arora SS, Hamilton G, et al. Multisite, multivendor validation of the accuracy and reproducibility of proton-density fat-fraction quantification at 1.5T and 3T using a fat-water phantom. Magn Reson Med. 2017;77(4):1516-24.
158. Grayev A, Reeder S, Hanna A. Use of chemical shift encoded magnetic resonance imaging (CSE-MRI) for high resolution fat-suppressed imaging of the brachial and lumbosacral plexuses. Eur J Radiol. 2016;85(6):1199-207.
159. Klose U. Measurement sequences for single voxel proton MR spectroscopy. Eur J Radiol. 2008;67(2):194-201.

160. Li G, Xu Z, Gu H, Li X, Yuan W, Chang S, et al. Comparison of chemical shift-encoded water-fat MRI and MR spectroscopy in quantification of marrow fat in postmenopausal females. J Magn Reson Imaging. 2017;45(1):66-73.
161. Valentin J. Basic anatomical and physiological data for use in radiological protection: reference values: ICRP Publication 89. Annals of the ICRP. 2002;32:1-277.
162. Johnson TR. Dual-energy CT: general principles. AJR Am J Roentgenol. 2012;199(5 Suppl):S3-8.
163. Arentsen L, Yagi M, Takahashi Y, Bolan PJ, White M, Yee D, et al. Validation of marrow fat assessment using noninvasive imaging with histologic examination of human bone samples. Bone. 2015;72:118-22.
164. Salas-Ramirez M, Lassmann M, Tran-Gia J. Quantification of the volume fraction of fat, water and bone mineral in spongiosa for red marrow dosimetry in molecular radiotherapy by using a dual-energy (SPECT/) CT. Z Med Phys. 2022;32:428-37.
165. Liu Z, Huang D, Zhang Y, Chang R, Zhang X, Jiang Y, et al. Accuracy and applicability of dual-energy computed tomography in quantifying vertebral bone marrow adipose tissue compared with magnetic resonance imaging. Insights Imaging. 2022;13(1):181.
166. Watchman CJ, Bourke VA, Lyon JR, Knowlton AE, Butler SL, Grier DD, et al. Spatial distribution of blood vessels and CD34+ hematopoietic stem and progenitor cells within the marrow cavities of human cancellous bone. J Nucl Med. 2007;48:645-54.
167. Bourke VA, Watchman CJ, Reith JD, Jorgensen ML, Dieudonnè A, Bolch WE. Spatial gradients of blood vessels and hematopoietic stem and progenitor cells within the marrow cavities of the human skeleton. Blood. 2009;114:4077-80.
168. Hough M, Johnson P, Rajon D, Jokisch D, Lee C, Bolch W. An image-based skeletal dosimetry model for the ICRP reference adult male—internal electron sources. Phys Med Biol. 2011;56:2309.
169. Gao D, Chang Q, Liu C, Farris K, Harvey K, McGann L, et al. Fundamental cryobiology of human hematopoietic progenitor cells I: Osmotic characteristics and volume distribution. Cryobiology. 1998;36:40-8.
170. Hardouin P, Rharass T, Lucas S. Bone marrow adipose tissue: to be or not to be a typical adipose tissue? Frontiers in endocrinology. 2016;7:85.
171. Matsui W, Brodsky R, Smith B, Borowitz M, Jones R. Quantitative analysis of bone marrow CD34 cells in aplastic anemia and hypoplastic myelodysplastic syndromes. Leukemia. 2006;20:458-62.

172. Black TJ, Cheviakov AF. 3DRSP: Matlab-based random sphere packing code in three dimensions. SoftwareX. 2022;18:101051.
173. d'Abadie P, Walrand S, Hesse M, Amini N, Lhommel R, Sawadogo K, et al. Accurate non-tumoral 99mTc-MAA absorbed dose prediction to plan optimized activities in liver radioembolization using resin microspheres. Phys Med. 2021;89:250-7.
174. Hermann AL, Dieudonne A, Ronot M, Sanchez M, Pereira H, Chatellier G, et al. Relationship of Tumor Radiation-absorbed Dose to Survival and Response in Hepatocellular Carcinoma Treated with Transarterial Radioembolization with (90)Y in the SARAH Study. Radiology. 2020;296(3):673-84.
175. Gabr A, Riaz A, Johnson GE, Kim E, Padia S, Lewandowski RJ, et al. Correlation of Y90-absorbed radiation dose to pathological necrosis in hepatocellular carcinoma: confirmatory multicenter analysis in 45 explants. Eur J Nucl Med Mol Imaging. 2021;48(2):580-3.
176. Hogberg J, Rizell M, Hultborn R, Svensson J, Henrikson O, Molne J, et al. Simulation Model of Microsphere Distribution for Selective Internal Radiation Therapy Agrees With Observations. Int J Radiat Oncol Biol Phys. 2016;96(2):414-21.
177. Alcocer-Ávila ME, Ferreira A, Quinto MA, Morgat C, Hindié E, Champion C. Radiation doses from 161 Tb and 177 Lu in single tumour cells and micrometastases. EJNMMI Phys. 2020;7:1-9.
178. Bernhardt P, Svensson J, Hemmingsson J, van der Meulen NP, Zeevaart JR, Konijnenberg MW, et al. Dosimetric analysis of the short-ranged particle emitter 161Tb for radionuclide therapy of metastatic prostate cancer. Cancers. 2021;13:2011.
179. Champion C, Quinto M, Morgat C, Fregonara PZ, Hindie E. Monte Carlo Comparison of Some beta- Isotopes of Interest for Targeted Radionuclide Therapy of Small Tumors: 177Lu, 67Cu, 47Sc and 161Tb. Journal of Nuclear Medicine. 2016;57(supplement 2):1014-.
180. Champion C, Quinto MA, Morgat C, Zanotti-Fregonara P, Hindié E. Comparison between three promising ß-emitting radionuclides, 67Cu, 47Sc and 161Tb, with emphasis on doses delivered to minimal residual disease. Theranostics. 2016;6(10):1611.
181. Hindie E, Zanotti-Fregonara P, Quinto MA, Morgat C, Champion C. Dose Deposits from 90Y, 177Lu, 111In, and 161Tb in Micrometastases of Various Sizes: Implications for Radiopharmaceutical Therapy. J Nucl Med. 2016;57(5):759-64.
182. Bodei L, Kidd M, Paganelli G, Grana CM, Drozdov I, Cremonesi M, et al. Long-term tolerability of PRRT in 807 patients with neuroendocrine tumours: the value and limitations of clinical factors. Eur J Nucl Med Mol Imaging. 2015;42(1):5-19.

183. Basic anatomical and physiological data for use in radiological protection: reference values. A report of age- and gender-related differences in the anatomical and physiological characteristics of reference individuals. ICRP Publication 89. Ann ICRP. 2002;32(3-4):5-265.
184. Santoro L, Mora-Ramirez E, Trauchessec D, Chouaf S, Eustache P, Pouget J-P, et al. Implementation of patient dosimetry in the clinical practice after targeted radiotherapy using [177Lu-[DOTA0, Tyr3]-octreotate. EJNMMI Res. 2018;8:1-13.
185. Marin G, Vanderlinden B, Karfis I, Guiot T, Wimana Z, Reynaert N, et al. A dosimetry procedure for organs-at-risk in (177)Lu peptide receptor radionuclide therapy of patients with neuroendocrine tumours. Phys Med. 2018;56:41-9.
186. Huizing D, Peters S, Versleijen MW, Martens E, Verheij M, Sinaasappel M, et al. A head-to-head comparison between two commercial software packages for hybrid dosimetry after peptide receptor radionuclide therapy. EJNMMI Phys. 2020;7:1-19.
187. Kim Y-i, Oh J, Yoo C, Ryoo B-Y, Ryu J-S. Prediction of absorbed dose by tumors and critical organs after Lu-177-DOTATATE therapy using pretherapeutic Ga-68-DOTATOC PET/CT. Journal of Nuclear Medicine. 2021;62(supplement 1):76-.
188. Vergnaud L, Giraudet A-L, Moreau A, Salvadori J, Imperiale A, Baudier T, et al. Patient-specific dosimetry adapted to variable number of SPECT/CT time-points per cycle for $^{177}$Lu-DOTATATE therapy. EJNMMI Physics. 2022;9(1):37.
189. Kamaldeep, Loharkar S, Das T, Basu S, Banerjee S. Estimation of Absorbed Doses of Indigenously Produced "Direct-route" Lutetium-177-[(177)Lu]Lu-DOTA-TATE PRRT in Normal Organs and Tumor Lesions in Patients of Metastatic Neuroendocrine Tumors: Comparison with No-Carrier-Added [(177)Lu]Lu-DOTA-TATE and the Trend with Multiple Cycles. Cancer Biother Radiopharm. 2022;37(3):214-25.
190. Sandström M, Garske-Román U, Granberg D, Johansson S, Widström C, Eriksson B, et al. Individualized dosimetry of kidney and bone marrow in patients undergoing 177Lu-DOTA-octreotate treatment. J Nucl Med. 2013;54:33-41.
191. Reidy-Lagunes D, Pandit-Taskar N, O'Donoghue JA, Krebs S, Staton KD, Lyashchenko SK, et al. Phase I Trial of Well-Differentiated Neuroendocrine Tumors (NETs) with Radiolabeled Somatostatin Antagonist 177Lu-Satoreotide Tetraxetan177Lu-Satoreotide Tetraxetan in Well-Differentiated NETs. Clinical Cancer Research. 2019;25:6939-47.

192. Nicolas G, Ansquer C, Lenzo N, Grønbæk H, Haug A, Navalkissoor S, et al. 1160O An international open-label study on safety and efficacy of 177Lu-satoreotide tetraxetan in somatostatin receptor positive neuroendocrine tumours (NETs): An interim analysis. Annals of Oncology. 2020;31:S771.
193. Cescato R, Waser B, Fani M, Reubi JC. Evaluation of 177Lu-DOTA-sst2 antagonist versus 177Lu-DOTA-sst2 agonist binding in human cancers in vitro. J Nucl Med. 2011;52:1886-90.
194. Baum RP, Zhang J, Schuchardt C, Müller D, Mäcke H. First-in-humans study of the SSTR antagonist 177Lu-DOTA-LM3 for peptide receptor radionuclide therapy in patients with metastatic neuroendocrine neoplasms: Dosimetry, safety, and efficacy. J Nucl Med. 2021;62:1571-81.
195. Falzone N, Fernandez-Varea JM, Flux G, Vallis KA. Monte Carlo Evaluation of Auger Electron-Emitting Theranostic Radionuclides. J Nucl Med. 2015;56(9):1441-6.
196. Tamborino G, Saint-Hubert D, Struelens L, Seoane DC, Ruigrok EA, Aerts A, et al. Cellular dosimetry of [177Lu] Lu-DOTA-[Tyr3] octreotate radionuclide therapy: the impact of modeling assumptions on the correlation with in vitro cytotoxicity. EJNMMI Phys. 2020;7:1-19.
197. Douglass M, Bezak E, Penfold S. Development of a randomized 3D cell model for Monte Carlo microdosimetry simulations. Med Phys. 2012;39(6):3509-19.